

# Hydrothermal Alteration on Composite Volcanoes -Mineralogy, Hyperspectral Imaging and Aeromagnetic Study of Mt Ruapehu, New Zealand

Gabor Kereszturi<sup>1</sup>, Lauren N Schaefer<sup>2</sup>, Craig Andrew Miller<sup>3</sup>, and Stuart Mead<sup>4</sup>

<sup>1</sup>Volcanic Risk Solutions, School of Agriculture and Environment, Massey University

<sup>2</sup>U.S. Geological Survey

<sup>3</sup>GNS Science

<sup>4</sup>Soil and Earth Sciences, School of Agriculture and Environment, Massey University

November 23, 2022

## Abstract

Prolonged volcanic activity can induce surface weathering and hydrothermal alteration that is a primary control on edifice instability, posing a complex hazard with its challenges to accurately forecast and mitigate. This study uses a frequently active composite volcano, Mt Ruapehu, New Zealand, to develop a conceptual model of surface weathering and hydrothermal alteration applicable to long-lived composite volcanoes. The rock samples were classified as non-altered, supergene argillic alteration, intermediate argillic alteration, and advanced argillic alteration. The first two classes have a paragenesis that is consistent with surficial infiltration and circulation of the low-temperature (40 degree C) neutral to mildly acidic fluids, inducing chemical weathering and formation of weathering rims on rock surfaces. The intermediate and advanced argillic alterations are formed from hotter (100 degree C) hydrothermal fluids with lower pH, interacting with the andesitic to dacitic host rocks. The distribution of weathering and hydrothermal alteration has been mapped with airborne hyperspectral imaging through image classification, while aeromagnetic data inversion was used to map alteration to several hundred meters depth. The joint use of hyperspectral imaging complements the geophysical methods since it can numerically identify hydrothermal alteration style. This study established a conceptual model of hydrothermal alteration history of Mt Ruapehu, exemplifying a long-lived and nested active and ancient hydrothermal system. This study highlights the need to combine mineralogical information, geophysical techniques and remote sensing to distinguish between current and ancient hydrothermal and supergene alteration systems, to indicate the most likely areas of future debris avalanche initiation.

## Hosted file

agusupportinginformation\_v1.docx available at <https://authorea.com/users/544322/articles/601635-hydrothermal-alteration-on-composite-volcanoes-mineralogy-hyperspectral-imaging-and-aeromagnetic-study-of-mt-ruapehu-new-zealand>

1  
2 **Hydrothermal Alteration on Composite Volcanoes –Mineralogy,**  
3 **Hyperspectral Imaging and Aeromagnetic Study of Mt Ruapehu, New**  
4 **Zealand**

5  
6 **Gabor Kereszturi<sup>1\*</sup>, Lauren N. Schaefer<sup>2,3</sup>, Craig Miller<sup>4</sup>, Stuart Mead<sup>1</sup>**

7  
8 <sup>1</sup>Volcanic Risk Solutions, Massey University, Palmerston North, 4474, New Zealand

9 <sup>2</sup>School of Earth and Environment, University of Canterbury, Christchurch, 8140, New Zealand

10 <sup>3</sup>U.S. Geological Survey, 1711 Illinois St., Golden, CO, 80401, USA

11 <sup>4</sup>GNS Science, Wairakei Research Centre, Taupo, 3353, New Zealand

12  
13 \*Corresponding author: Gabor Kereszturi ([G.Kereszturi@massey.ac.nz](mailto:G.Kereszturi@massey.ac.nz))

14  
15  
16 **Key Points:**

- 17
- 18 • Surface weathering and hydrothermal mineralogy was constrained using VNIR and  
19 SWIR reflectance spectroscopy and SEM-EDS analysis
  - 20 • Combination of airborne hyperspectral image analysis and aeromagnetic data inversion  
21 mapped surface and buried hydrothermal alteration on Mt Ruapehu volcano
  - 22 • Complex hydrothermal evolution of Mt Ruapehu is revealed using geophysical imaging  
23 techniques combined with surface alteration mineralogy

24  
25  
26  
27  
28  
29  
30  
31  
32  
33  
34  
35  
36  
37  
38  
39  
40  
41  
42  
43  
44  
45  
46  
47  
48  
49  
50  
51  
52  
53  
54  
55  
56  
57  
58  
59  
60  
61  
62  
63  
64  
65  
66  
67  
68

## Abstract

Prolonged volcanic activity can induce surface weathering and hydrothermal alteration that is a primary control on edifice instability, posing a complex hazard with its challenges to accurately forecast and mitigate. This study uses a frequently active composite volcano, Mt Ruapehu, New Zealand, to develop a conceptual model of surface weathering and hydrothermal alteration applicable to long-lived composite volcanoes. The rock samples were classified as non-altered, supergene argillic alteration, intermediate argillic alteration, and advanced argillic alteration. The first two classes have a paragenesis that is consistent with surficial infiltration and circulation of the low-temperature (<40 °C) neutral to mildly acidic fluids, inducing chemical weathering and formation of weathering rims on rock surfaces. The intermediate and advanced argillic alterations are formed from hotter ( $\geq 100$  °C) hydrothermal fluids with lower pH, interacting with the andesitic to dacitic host rocks. The distribution of weathering and hydrothermal alteration has been mapped with airborne hyperspectral imaging through image classification, while aeromagnetic data inversion was used to map alteration to several hundred meters depth. The joint use of hyperspectral imaging complements the geophysical methods since it can numerically identify hydrothermal alteration style. This study established a conceptual model of hydrothermal alteration history of Mt Ruapehu, exemplifying a long-lived and nested active and ancient hydrothermal system. This study highlights the need to combine mineralogical information, geophysical techniques and remote sensing to distinguish between current and ancient hydrothermal and supergene alteration systems, to indicate the most likely areas of future debris avalanche initiation.

## Plain Language Summary

Groundwater heated by shallow intrusive bodies beneath an volcano can contribute heat and magmatic gasses to the groundwater. The magmatic contributions, such as sulfur dioxide, can make groundwater acidic. When the acidic groundwater rises to the surface, it chemically interacts and changes volcanic rocks, leading to hydrothermal alteration. This alteration can weaken rocks by depositing clay minerals in fractures and pore-space, and in turn inducing edifice collapse hazards. This contribution integrates mineralogy, hyperspectral remote sensing and geophysical methods to understand the hydrothermal alteration history of a seemingly unaltered volcano, Mt Ruapehu, New Zealand. Ground sampling indicates alteration mineralogy is dominated by sulfides and sulfates. Hyperspectral remote sensing measures reflected sunlight from the Earth's surface, allowing quantitative discrimination and mapping of surface minerals at high resolution using image classification. The surface alteration was jointly analyzed with the aeromagnetic inversion models to understand underground hydrothermal alteration. Aeromagnetic data is sensitive to iron-bearing, magnetic minerals that are often dissolved by hydrothermal fluids, leaving low magnetic anomalies. The combination of these methods allowed a detailed conceptualization of alteration history of Mt Ruapehu during the last 200,000 years. This conceptual model will be used to assess natural hazards associated with flank collapses using numerical models.

## 1. Introduction

69 Interaction of the magmatic heat and gasses ( e.g. mostly Cl, SO<sub>2</sub>, H<sub>2</sub>O, CO<sub>2</sub>) drives  
70 infiltrating surface and circulating groundwater to ascend through the volcanic host rocks while  
71 leaching primary alkali (Na, K) and alkaline earth metals (Mg, Ca), replacing existing mineral  
72 phases and precipitating new secondary minerals at shallower depths (Ganino et al., 2019; Hynek  
73 et al., 2013; Rowe and Brantley, 1993; Rye et al., 1992). Acid-sulfate alteration forms typical  
74 intermediate and advanced argillic mineral assemblages, including phyllosilicates (Dill, 2016;  
75 Hynek et al., 2013), sulfates (Rye et al., 1992; Zimbelman et al., 2005), sulfides, and native sulfur  
76 (Inostroza et al., 2020; Piochi et al., 2015). The majority of hydrothermal alteration occurs beneath  
77 the surface in hypogene conditions; however, mineral assemblages formed under hypogene  
78 conditions are often subject to supergene weathering and erosion which can replace some of the  
79 metastable hydrothermal minerals under atmospheric pressure and temperature conditions,  
80 including dickite, anhydrite, sulfur and pyrite (Fernández-Caliani et al., 2004; John et al., 2008;  
81 Scott, 1990; Zimbelman et al., 2005). This commonly results in mineral imprinting, making  
82 interpretations of the original hydrothermal condition, fluid composition and pH challenging,  
83 particularly on complex and long-lived volcanic systems.

84 Hydrothermal alteration results in economic resources, such as Au, Ag, and base metal  
85 deposits; however, it also changes rock mechanical and geotechnical properties (del Potro and  
86 Hürlimann, 2009; Pola et al., 2014), promoting flank instability (Finn et al., 2001; Heap et al.,  
87 2015; John et al., 2008; López and Williams, 1993; Norini et al., 2020; Schaefer et al., 2015) and  
88 increasing the likelihood of phreatic eruptions (Mayer et al., 2017; Pardo et al., 2014).  
89 Hydrothermal alteration primarily reduces rock strength (del Potro and Hürlimann, 2009;  
90 Farquharson et al., 2019), and changes permeability within the volcanic edifice (Mordensky et al.,  
91 2019b), which may locally elevate pore-pressure promoting edifice flank instabilities (Ball et al.,  
92 2018; Collard et al., 2020; Reid, 2004). Flank instabilities, and the resulting mass flow events  
93 triggered by gravity, weather events, volcanic eruptions, magmatic intrusions, and earthquakes  
94 (Capra, 2006; Procter et al., 2014; Schaefer et al., 2018) can result in far-reaching and potentially  
95 dangerous volcanic hazards downstream from volcanoes (Finn et al., 2001).

96 Geological mapping and quantification of hydrothermal alteration in volcanic systems have  
97 traditionally been carried out using ground and field geological mapping, combined with Scanning  
98 Electron Microscopy (SEM), X-Ray Diffraction (XRD) and X-ray fluorescence (XRF), and  
99 isotope and fluid inclusions studies, among others, to constrain the paragenesis of the alteration  
100 mineral suites (Ball et al., 2013; Christenson and Wood, 1993; John et al., 2008; Nuñez-Hernández  
101 et al., 2020; Piochi et al., 2019; Rye, 2005; Zimbelman et al., 2005). Multispectral satellite remote  
102 sensing in the Visible and Near Infrared (VNIR – 300-1000 nm) and Shortwave Infrared (SWIR –  
103 1000-2500 nm) is often used to upscale mapping efforts, using Landsat series (Mia and Fujimitsu,  
104 2012; Wright et al., 2001), Advanced Spaceborne Thermal Emission and Reflection Radiometer –  
105 ASTER (Galvão et al., 2005; Rowan and Mars, 2003), and WorldView constellation (Kruse et al.,  
106 2015). Lately, hyperspectral remote sensing is becoming available for mineral alteration mapping,  
107 improving the differentiation among key indicator minerals such as alunite, jarosite, kaolinite,  
108 montmorillonite and illite, and mica, offering a cost-effective but highly sophisticated  
109 technological solution (Carrino et al., 2018; Crosta et al., 1998; Crowley et al., 2003; Hellman and  
110 Ramsey, 2004; Kereszturi et al., 2018; Swayze et al., 2014; van der Meer, 2004). However, optical  
111 remote sensing approaches are limited to quantify only the surface manifestation of hydrothermal  
112 alteration and weathering, hampering these techniques to be used for hazard assessment of  
113 geophysical mass flow.

114 Complementing ground and remote sensing methods, geophysical techniques, including  
115 electromagnetic resistivity, gravity and aeromagnetic surveys (Finn et al., 2018; Miller and  
116 Williams-Jones, 2016), magnetotelluric surveys (Abdallah et al., 2020; Bowles-Martinez and  
117 Schultz, 2020; Jones et al., 2008; Matsunaga et al., 2020), seismicity (Pu et al., 2020), moun  
118 imaging (Le Gonidec et al., 2019) have also been used to infer internal architecture, and locate  
119 hydrothermal fluids and zones of demagnetization of the host rock. These survey methods are often  
120 complemented with numerical methods and spring and gas chemistry data to gain insights into the  
121 thermal and chemical evolution of shallow magmatic-hydrothermal systems (Berlo et al., 2020;  
122 Collard et al., 2020; Gresse et al., 2018; Miller et al., 2020a). Therefore, geophysical inversion and  
123 numerical methods can add the depth component to quantify hydrothermal alteration processes  
124 and volumes of altered rock masses, contributing important inputs to mass flow initiation and run-  
125 out models and hazard assessment (Finn et al., 2018; Finn et al., 2001; Rosas-Carbajal et al., 2016).

126 Both geophysical and optical remote sensing approaches have been demonstrated to be  
127 useful for mapping hydrothermal alteration products. However, the joint use of such methods is  
128 seldomly presented on composite volcanoes to fingerprint hydrothermal alteration processes on  
129 the surface and depth. This study aims, therefore, to explore the hydrothermal alteration history of  
130 a long-lived and complex andesitic composite volcano, Mt Ruapehu, New Zealand, using a novel  
131 combination of mineralogical, hyperspectral and geophysical imaging techniques. The detailed  
132 reconstruction of the hydrothermal alteration history and conceptual model can provide inputs to  
133 predict edifice instabilities and associated geophysical mass flow hazards around composite  
134 volcanoes.

## 135 136 **2. Geological Setting** 137

138 The southern part of the Taupo Volcanic Zone contains Mt Tongariro and Mt Ruapehu  
139 volcanoes and several smaller inactive volcanic centers, which collectively form the Tongariro  
140 Volcanic Complex (Fig. 1A). Mt Ruapehu, 2797 m a.s.l. and 110 km<sup>3</sup>, is a frequently active  
141 andesite-dacite volcano (Hackett and Houghton, 1989), formed via back-arc volcanism behind an  
142 active subduction zone at the Australian and Pacific plate boundary (e.g. Stern et al., 2006; Wallace  
143 et al., 2004).

144 The first deposit originated from Mt Ruapehu is dated to around 340 ky ago (Hackett and  
145 Houghton, 1989; Price et al., 2012), preserved within distal catchment areas as river aggradation  
146 terraces (e.g. Tost et al., 2015). The stratigraphic framework of Mt Ruapehu comprises four  
147 formations, on the basis of geochronology, geochemistry and stratigraphic relationships,  
148 pinpointing distinct spatial-temporal stages of volcano evolution (Fig. 1A): Te Herenga (200 to  
149 150 ka), Wahianoa (166-80 ka), Mangawhero (50-15 ka) and Whakapapa (<15 ka) formations  
150 (Conway et al., 2016; Gamble et al., 2003; Hackett and Houghton, 1989; Price et al., 2012;  
151 Townsend et al., 2017). The only major hiatus in activity is from 80 to 50 ky, which was a period  
152 of erosion and edifice instabilities (Townsend et al., 2017).

153  
154  
155

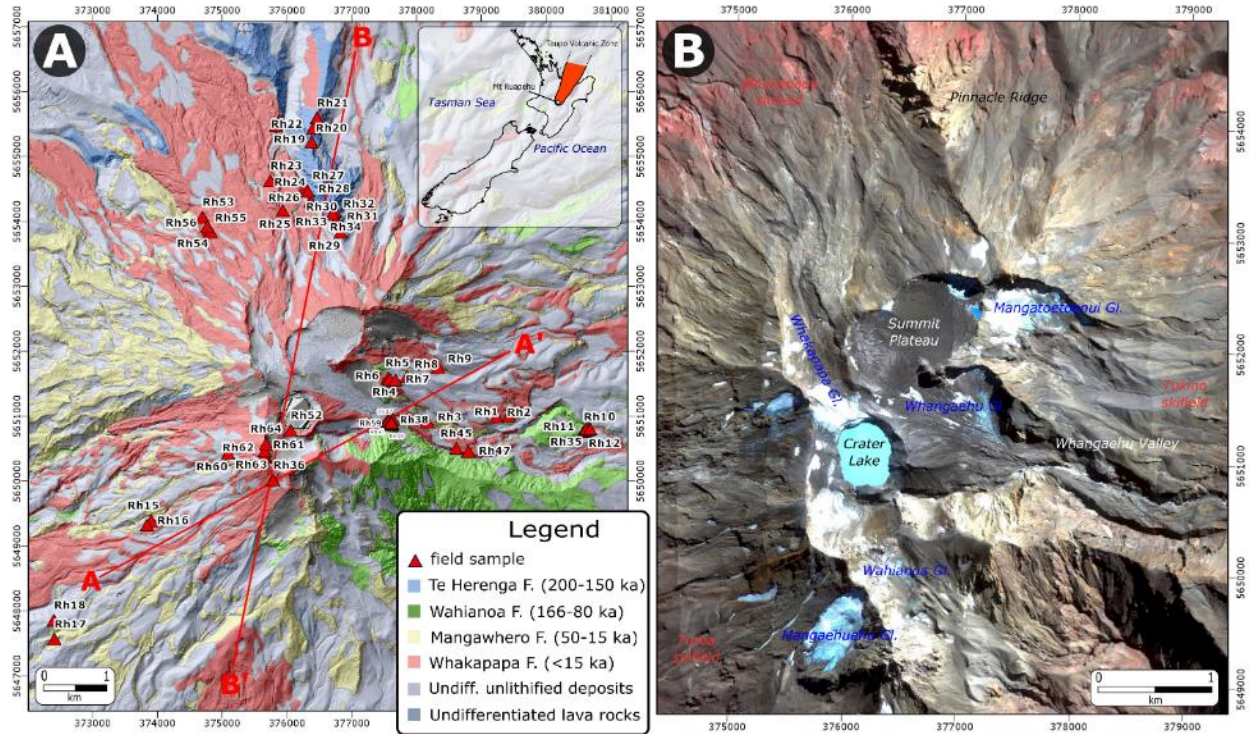


**Figure 1.** (A) A simplified geological map of Mt Ruapehu, with the major geological formations after Townsend et al. (Townsend et al., 2017), draped over a hillshade model. The red triangles show the location of the physical samples collected in this study. (B) Infrared-colored composite image of the airborne hyperspectral imagery ( $R = 860.1$  nm;  $G = 650.2$  nm,  $B = 550.7$  nm) with the locations mentioned in the text.

The whole-rock chemistry of Mt Ruapehu varies between basaltic andesite and dacites (Price et al., 2012). Rock textures at Mt Ruapehu are mainly porphyritic with phenocryst abundances averaging 35-55% (Price et al., 2012); however, some lava flows exhibit aphyric texture. The main phenocrysts in decreasing abundance are plagioclase (8-39 vol%), clinopyroxene (2-14 vol%), orthopyroxene (2-10 vol%), magnetite and titanomagnetite (1-6 vol%), as well as rare occurrences of olivine and amphiboles (Conway et al., 2018; Gamble et al., 1999; Graham and Hackett, 1987; Nakagawa et al., 1999; Price et al., 2012). See detailed summary in Table S1. The composition of the plagioclase and pyroxene phenocrysts show differences within the main lithologic units, highlighting a changing magmatic source and edifice evolution over time (Conway et al., 2018; Kilgour et al., 2013).

The current volcanic edifice is made of mostly lava flows and their auto-breccias, with minor exposed volcanoclastic deposits, such as lahar, debris avalanche and tephra fall deposits (Conway et al., 2016; Townsend et al., 2017). Such lava flows seldomly reach the extensive ring plain around the volcanoes which preserved an extensive record of debris flows, debris avalanches, hyper-concentrated flows with interbedded local andesitic and distal rhyolitic tephra (Donoghue and Neall, 1996; Pardo et al., 2012). Mt Ruapehu has produced 8-10 debris avalanches in the last 340 ky. The last two debris avalanches, Murimotu (9.5 ky) and Mangaio (4.6 ky) affected the NW and E sides, and reached ca. 15 and 25 km distance, respectively (Donoghue and Neall, 2001; Palmer and Neall, 1989).

183 A recent period of magmatic activity occurred between September and November 1995,  
184 and June and July 1996, producing mild Strombolian to violent phreatomagmatic eruptions  
185 (Cronin et al., 1997; Johnston et al., 2000; Nakagawa et al., 1999). The 1995-96 and 2007 eruptions  
186 disrupted the top parts of the hydrothermal system, providing otherwise inaccessible samples to  
187 characterize the physico-chemical state of the host rock and hydrothermal under the currently  
188 active Crater Lake (Christenson, 2000; Christenson et al., 2010; Christenson and Wood, 1993).

189 A previous magnetotelluric survey data was used to model the electrical resistivity structure  
190 of the upper flanks of Mt Ruapehu and its surroundings, indicating hydrothermally altered rocks  
191 located under the Summit Plateau (Ingham et al., 2009; Jones et al., 2008). Two higher resistivity  
192 zones (20-60  $\Omega$  m) located under the Northern part of the Summit plateau at 200-500 m, and 1000-  
193 1500 m depths, are interpreted to be due to changing alteration mineralogy from smectite-illite to  
194 chlorite-rich zones (Jones et al., 2008). This region was further imaged using aeromagnetic data  
195 inversion and interpreted to be smaller demagnetized zones, corresponding to hydrothermally  
196 altered rocks (Miller et al., 2020b). Besides Crater Lake, there is no known active hydrothermal  
197 system on Mt Ruapehu; however, older parts of the Mt Ruapehu indicates extensive hydrothermal  
198 alteration history, such as the Te Herenga Formation (Mordensky et al., 2019a).

### 199 **3. Methods and Materials**

#### 200 3.1. Field Sampling and Lab Analytics

201  
202  
203 A total of 64 samples were collected during field campaigns between 2017 and 2019 (Fig.  
204 1A). The samples are from lava flows (interior core and brecciated exterior), and tephra deposits  
205 and range from fresh to extensively altered. Some of the samples represent subsurface lithologies  
206 (upper 200 m), brought to the surface by the 2007 eruption induced lahar and the ballistics from  
207 the 1995-96 eruption. Samples were analyzed using lab-based reflected light spectroscopy, optical  
208 microscopy, and Scanning Electron Microscope (SEM) equipped with Energy Dispersive X-ray  
209 spectroscopy (EDS).

210 Lab-based reflectance spectroscopy was completed using a FieldSpec 4 Hi-Res  
211 spectroradiometer, equipped with a Hi-Brightness contact probe with a sampling footprint of 10  
212 mm in diameter. The samples were air-dried at 40 °C for 24 hours before analysis to ensure samples  
213 were dry. The spectral readings were calibrated against a white Spectralon Diffuse Reflectance  
214 Standard. Spectra measurements were completed at 2-7 “spots” on each specimen, which assured  
215 representative sampling of the variation of the alteration within each sample. Each of these “spots”  
216 included at least 100 spectral measurements. All spectral measurements were then averaged using  
217 View Spec Pro software and later exported into a spectral library. When an alteration rim/crust  
218 was present on a sample, the interior and outer rim were analyzed separately. The averaged spectral  
219 reflectance was used to recognize the typical mineral association within the samples using  
220 continuum removed spectral curves (Clark and Roush, 1984). The wavelength of the absorption  
221 features (i.e. reflectance lows) was matched manually with the USGS Spectral Library Version 7  
222 (Kokaly et al., 2017), as well as automatically using a Spectral Feature Fitting approach  
223 implemented in ENVI (Clark et al., 1990). A list of key spectral absorption features and  
224 descriptions are summarized in Table S2.

225 A subset of the samples was prepared for thin section, Scanning Electron Microscope (SEM)  
226 and Energy-dispersive X-ray Spectroscopy (EDS) for petrographic and geochemical analysis.  
227 These samples were cut, mounted onto glass slides and then ground to 30  $\mu$ m and polished for  
228 optical microscopy, while other samples were ground to about 100  $\mu$ m, and polished for SEM-

229 EDS analysis. The latter batch was carbon-coated and imaged using ThermoFisher Scientific™  
230 FEI Quanta 200 Environmental Scanning Electron Microscope operated in Back-Scattered  
231 Electron (BSE) mode under accelerating voltage of 20 kV, with a working distance of 10 mm, at  
232 the Massey University's Manawatu Imaging Centre. BSE equipped with an EDAX-EDS system  
233 was used to identify element abundance to characterize rock alteration types and secondary  
234 mineralogy.

235 Magnetic susceptibility measurements were made on tephra and rock outcrop and hand  
236 specimens using a Terraplug KT-10 v2 magnetic susceptibility meter. The Terraplug was held in  
237 direct contact with the surface of each sample on a flat surface if possible, measured three times,  
238 and averaged to produce one value per sample.

239

240

### 241 **3.2. Hyperspectral Imaging Surveys**

242

243 Aerial surveys were completed using a Cessna 185 survey aircraft, with two integrated  
244 imaging systems onboard, between 10:25-12:45 NZST on 31 March 2018. The survey aircraft  
245 hosted a Specim AisaFENIX hyperspectral imaging system, alongside a Nikon D810 digital  
246 single-lens reflex camera with a 35 mm lens. The aircraft was flown at 3300 feet above the ground,  
247 capturing N-S orientation survey strips with 410 m line spacing.

248 The GPS-tagged digital photos had a maximum ground resolution of 13.9 cm. They were  
249 captured with 60% side- and forward overlaps. This imagery was to create a structure-from-motion  
250 Digital Surface Model (James and Robson, 2012; Westoby et al., 2012). The RAW imagery was  
251 converted to JPEG to perform the initial image matching in Pix4D software package. This was  
252 followed by georectification using 3D ground control points from high-resolution aerial  
253 photographs, taken in 2016, from Land Information New Zealand, and existing 10 m terrain  
254 models captured by Horizons Regional Council. This workflow resulted in a 50 cm bare-ground  
255 Digital Terrain Model (DTM), and 50 cm an orthophoto mosaic. Both were used to process and  
256 co-register the coarser-resolution hyperspectral imagery.

257 The AisaFENIX hyperspectral sensor is a push-broom, full-spectrum imaging system, along  
258 with an Oxford Survey+ Global Position System and Inertial Measurement Unit (Pullanagari et  
259 al., 2016). It captures reflected light between 377 and 2500 nm with variable spectral sampling  
260 intervals of 3.3-5.7 nm for VNIR bands and of 11 nm for the SWIR bands. It has a full-width-at-  
261 half-maximum between 3.2–12.2 nm. The Field of View is 32.2°, while the Instantaneous Field of  
262 View is 0.084°. The data has 448 spectral bands with a ground resolution of 1.5 m. The raw  
263 hyperspectral sensor measurements are converted to radiance ( $W \cdot sr^{-1} \cdot m^{-2}$ ) using sensor-specific  
264 gain and offset values, provided by Specim Ltd, Finland. The radiance imagery is corrected for  
265 atmospheric effect using ATCOR-4 algorithm, performed on the raw imaging geometry (Richter  
266 and Schläpfer, 2002). The atmospheric correction parameters were identical to Kereszturi et al.  
267 (2018). The atmospherically corrected imagery represents surface reflectance values that can be  
268 compared with spectral libraries or with other survey data. The atmospherically corrected  
269 reflectance imagery was geocoded using PARGE (Schläpfer and Richter, 2002). Since the  
270 hyperspectral imagery was captured with standard GPS positioning ( $\pm 6-8$  m at  $2\sigma$ ), there are often  
271 misalignments and shift to *X* and *Y* directions by up to 10 m. This was reduced by co-registering  
272 all image strips to the high-resolution orthophoto. The Root Mean Squared Error of the co-  
273 registration was around  $<2$  m. The imagery was mosaiced, and then spectrally smoothed to reduce  
274 noise.

275 The hyperspectral imagery can be used to map the surface spatial distribution of  
276 hydrothermally altered mineral packages (Carrino et al., 2018; Murphy et al., 2015; Rogge et al.,  
277 2014; Zabcic et al., 2014), using supervised image classification. This requires training and  
278 validation data to be identified. This study uses the hydrothermal alteration mineralogy and their  
279 sample location as well as field observations to develop training and validation populations, split  
280 at 50-50% for the supervised image classification. The total area was split into 5 rock alteration  
281 classes based on the alteration mineralogy (e.g. unconsolidated-unaltered, unaltered lava rocks,  
282 supergene argillic alteration, intermediate-, and advanced argillic alteration types), and 3 general  
283 classes (e.g. water, ice/glacier and shadow). The alteration types were based on the observed  
284 mineralogy in the collected samples. This study used Random Forest classification (Breiman,  
285 2001), which is effective at reducing overfits due to highly co-linear data (i.e. hyperspectral  
286 imagery), while also being time-efficient, and yielding accurate results (Belgiu and Drăguț, 2016;  
287 Kereszturi et al., 2018; Pal, 2005). Random Forest algorithm constructs decision trees using a  
288 subset of the training data and variables (i.e. spectral bands). Each tree is expanded until either the  
289 maximum number of input data used or they reached the minimum impurity value (i.e. 0), based  
290 on the calculated Gini impurity measure (Belgiu and Drăguț, 2016; Breiman, 2001). In this study,  
291 the total number of tree models was 500, and at each split of the inputs, the square-root of input  
292 total variables (i.e. 21 bands) was used. The class values were assigned using majority voting  
293 procedure based on the individual tree's prediction. The resultant classification image was assessed  
294 using independent validation population, through calculating the overall accuracy and an error  
295 matrix of user's and producer's accuracies (Liu et al., 2007).

296

### 297 **3.3. Helicopter borne Aeromagnetic Survey**

298

299 A helicopter-based aeromagnetic survey was carried out two weeks after the hyperspectral  
300 surveys in April 2018. We collected 800 km of magnetic data with a Geometrics G822A Ce-  
301 vapor magnetometer flown at 50 m above ground at 250 m-spaced flight lines which we reduced  
302 to 125 m over the Pinnacles and Summit Plateau. Sampling the magnetic field at 10 Hz results in  
303 a magnetic field value every 2 m. We corrected for diurnal variations using a local base  
304 magnetometer outside the survey region and subtracted the International Geomagnetic Reference  
305 Field (IGRF) at each data point location using the IGRF 2005 model. The data were levelled  
306 using widely spaced tie lies to minimize cross over difference and were gridded for visualization  
307 at 20 % of the line spacing using a minimum curvature algorithm (see Miller et al. (2020b) for  
308 full details).

309 To map the spatial distribution of magnetic and non-magnetic rocks within Mt Ruapehu  
310 volcano, a magnetic vector inversion algorithm was used, which is implemented in the SimPEG  
311 inversion framework package (Cockett et al., 2015; Fournier et al., 2020; Miller et al., 2020b).  
312 The inversion accounts for remanent magnetism, common in volcanic rocks, by solving for both  
313 the amplitude and direction of magnetization. The inversion returns a 3D model of apparent  
314 susceptibility that we interpret in terms of altered versus fresh rocks, where high apparent  
315 susceptibility typically reflects unaltered rocks and low apparent susceptibility increasingly  
316 altered rocks. The inversion model uses a mesh with minimum dimensions of 50×50×25 m or  
317 25×25×10 m over the Pinnacle Ridge and Summit Plateau areas. The typical apparent  
318 susceptibility values recorded from the model range from 0 to 0.05 SI, which can be interpreted  
319 as a degree of hydrothermal alteration, from fully demagnetized/unaltered to magnetic/fresh rocks,  
320 respectively (Miller et al., 2020b).

321  
322  
323  
324  
325  
326  
327  
328  
329  
330  
331  
332  
333  
334  
335  
336  
337  
338  
339  
340  
341  
342  
343  
344  
345  
346  
347  
348  
349  
350  
351  
352

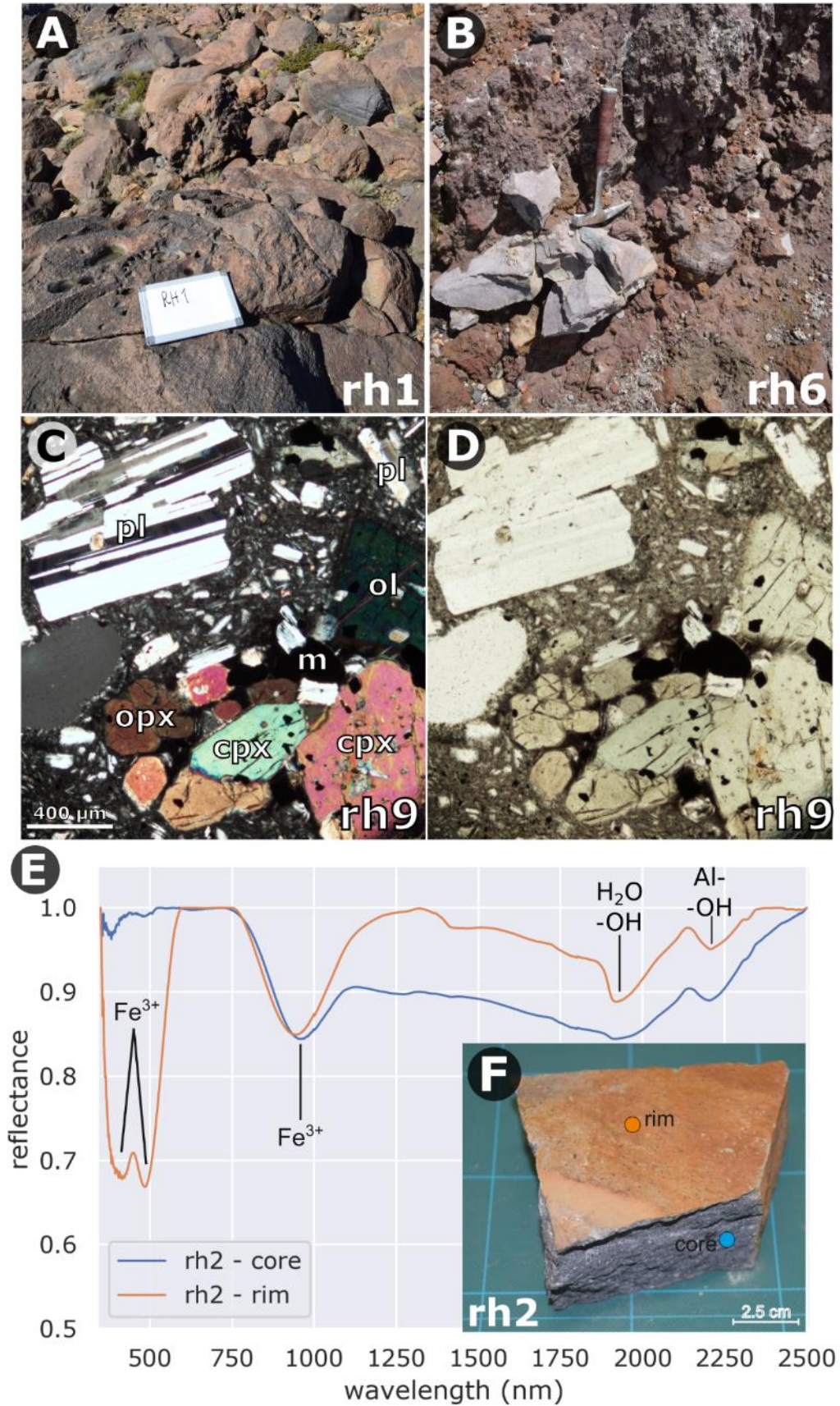
## 4. Results

### 4.1. Alteration Mineralogy

Based on the physical samples were grouped based on their alteration mineral phases mineralogy: (1) non-altered rock/deposits with minor surface weathering, (2) supergene argillic alteration with weathering rim, (3) intermediate argillic alteration and superimposed surface weathering, and (4) advanced argillic alteration. This classification scheme is based on the presence and absence of alteration minerals that represent distinct physico-chemical alteration domains (John et al., 2019; John et al., 2008; Rye et al., 1992; Zimbelman et al., 2005).

#### 4.1.1. Non-altered Lithologies with minor weathering

The non-altered lithologies frequently occur on blocky lava flows with auto-brecciated horizons (Figs 2A-B) and are characterized by absorption at wavelengths of 420, 480, 500-560, 1912, 2200 nm, and occasionally  $\pm 660$ ,  $\pm 950$ ,  $\pm 1430$  nm (e.g. rh1, rh2, rh4-9). In thin section, the studied samples show mostly fresh porphyritic, and rarely aphyric and vitrophyric textures (Figs 2C-D). The samples have about 30-50 vol% phenocrysts of plagioclase, clinopyroxene and orthopyroxene, various amounts of Ti-rich magnetite, and rarely olivine (Figs 2C-D). The phenocrysts are often euhedral to subhedral and occasionally show glomerophyric appearance. Some of the phenocrysts show chemical zonation, melt inclusions and sharp crystal boundaries, indicating their unaltered and fresh origin. The groundmass is made of tabular plagioclase microlites and volcanic glass. Some samples have a thin ( $\leq 1$  mm) yellow to brown colored alteration rim, in which the groundmass is often replaced by secondary minerals, including phyllosilicates. The phenocryst phase appears to be still fresh (Figs 2C-D), but rarely Ti-magnetite crystals show trellis-type lamellae structures, especially within weathering rims. This can potentially indicate either high-temperature exsolution and oxidation during cooling (e.g. Buddington and Lindsley, 1964; Tan et al., 2016) or due to hydrothermal alteration and surface weathering (e.g. van Hinsberg et al., 2010). The measured magnetic susceptibilities of this group range from 0.002 to 0.03 SI (Miller et al., 2020b), reflecting a wide range of variability of the (Ti-) magnetite content on Mt Ruapehu (Price et al., 2012).



354  
355 **Figure 2.** (A-B) Field photos of the fresh non-altered outcrop, and (C-D) thin section photographs  
356 of a fresh lava sample under cross-polarized light in C and plane-polarized light in D.  
357 Abbreviations: plg – plagioclase, opx – orthopyroxene, cpx – clinopyroxene, o – olivine, m –  
358 magnetite. (E) Spectral reflectance profiles of the inner core and rim of rh2 sample (F). The main  
359 elements and element-bonds are indicated the cause of the light absorption. The reflectance values  
360 have been normalized using continuum removal (Clark and Roush, 1984).

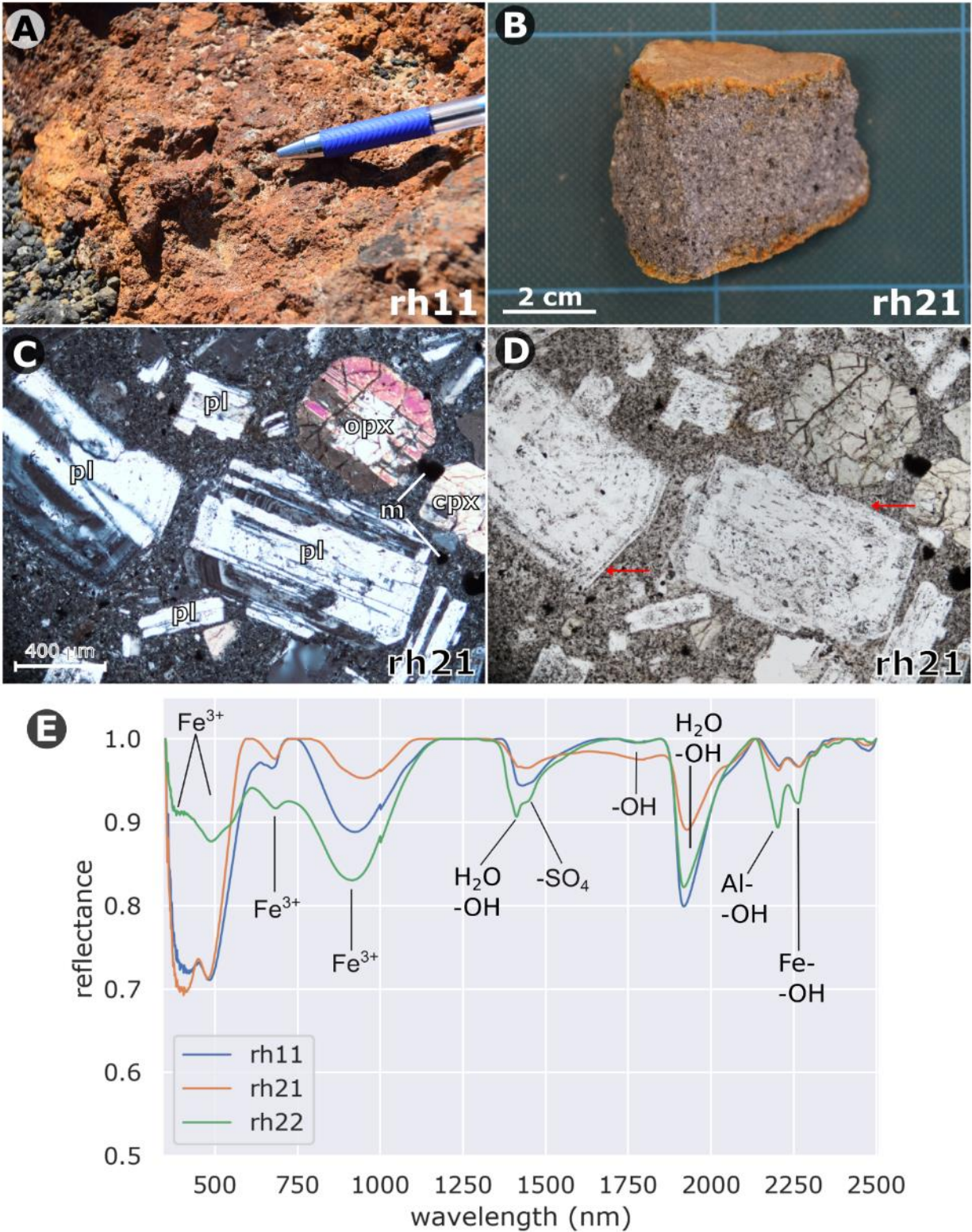
361  
362 The position of the absorption in the VNIR and SWIR regions can be explained by oxidation  
363 of primary mineralogy (e.g. magnetite, pyroxene) and limited, but detectable development of  
364 secondary clay minerals (e.g. mostly in the groundmass), with and without alteration rims (e.g.  
365 Fig. 2E). Such absorption is due to the presence of hydrous phases (e.g. 1430, 1912 and 2200-2350  
366 nm, and state transition from  $\text{Fe}^{2+}$  to  $\text{Fe}^{3+}$  (e.g. between 400-1000 nm) (Hunt and Ashley, 1979)).  
367 Typically, the alteration rims contain more secondary minerals, such as goethite,  $\pm$ ferrihydrite,  
368  $\pm$ phyllosilicate and hematite. This observation is consistent for both tephra, breccia and lava rocks  
369 (e.g. Table S3). Moreover, most of the samples show similar spectral reflectance for both the core  
370 and rim in the SWIR region (e.g. rh19 - Tawhainui lava flow, Iwikau Member, Whakapapa  
371 formation), indicating the overall fresh, young ( $\leq 50$  ky) and unaltered state of the samples.

#### 372 373 4.1.2. Supergene Argillic Alteration

374  
375 These samples have additional spectral features to the unaltered lithologies, at around 650,  
376 950, 1270, 1430, 1770, 2050, 2260, 2480 nm (e.g. rh10-11, rh21-23). These are consistent with  
377 Fe-oxides (e.g. goethite, hematite), with occasional jarosite and phyllosilicate phases, and are often  
378 limited to the alteration rim of the samples (Fig 3A). The alteration rims are often thicker than in  
379 the non-altered samples ( $>2$  mm). The core is often comprised of fresh phenocrysts and micro-  
380 phenocryst populations characterized by sharp boundaries and sub- to euhedral crystals, lacking  
381 any pervasive alteration in the core of the samples (Figs 3C-D). This freshness of phenocrysts and  
382 micro-phenocrysts are also accompanied by magnetic susceptibilities, ranging from 0.005 to 0.02  
383 SI (Miller et al., 2020b).

384 The spectroscopic data indicate the presence of both goethite ( $\text{FeO}(\text{OH})$ ) and hematite  
385 ( $\text{Fe}_2\text{O}_3$ ) on Mt Ruapehu, with a dominance of goethite. The formation of such alteration minerals  
386 is strongly pH-dependent. Acidic ( $\text{pH} = 2-5$ ) and alkaline conditions ( $\text{pH} = 10-14$ ) favor the  
387 formation of goethite, while neutral pH promotes the formation of hematite (e.g. Schwertmann  
388 and Murad, 1983). However, both minerals can occur on the same hand specimen, indicating a  
389 highly heterogeneous occurrence of those minerals on a cm-scale.

390  
391



392  
393

394 **Figure 3.** (A-B) Field and sample photos of the supergene argillic alteration showing various  
395 surface colorations and oxidations at outcrop scale. (C-D) Thin section photographs showing  
396 fresh phenocryst population with sharp contact (red arrow) viewed under cross-polarized light in

397 C and plane-polarized light in D. Abbreviations: plg – plagioclase, opx – orthopyroxene, cpx –  
398 clinopyroxene, m – magnetite. (E) Spectral reflectance profiles of representative samples  
399 showing supergene argillic alteration minerals.

400  
401 Jarosite ( $\text{KFe}_3(\text{SO}_4)_2(\text{OH})_6$ ) is common in the alteration rims, suggesting a supergene origin  
402 as a weathering product of Fe-bearing rocks. It often forms from oxidation products under acidic  
403 conditions, and frequently forms in concert with ferric oxyhydroxides (Bishop and Murad, 2005).  
404 The jarosite phase (e.g. absorption feature at 2265 nm; Fig. 3E) is observed more often within the  
405 Te Herenga Formation (e.g. rh21-23) than in the Wahianoa Formations (e.g. rh10-11). This is  
406 consistent with the geochemistry of the original rocks (e.g. increased K and Fe content in the Te  
407 Herenga Formation; Table S1). The mineral assemblages are consistent with a paragenesis of a  
408 supergene argillic alteration and oxidation under atmospheric conditions, forming diverse  
409 alteration rims, depending on the primary rock geochemistry, and the exposure time to alteration  
410 processes (>50 ky). This process can be driven by metasomatism of K-bearing plagioclase phases  
411 by slightly acidic surface waters, causing surface weathering (e.g. Vasconcelos and Conroy, 2003).

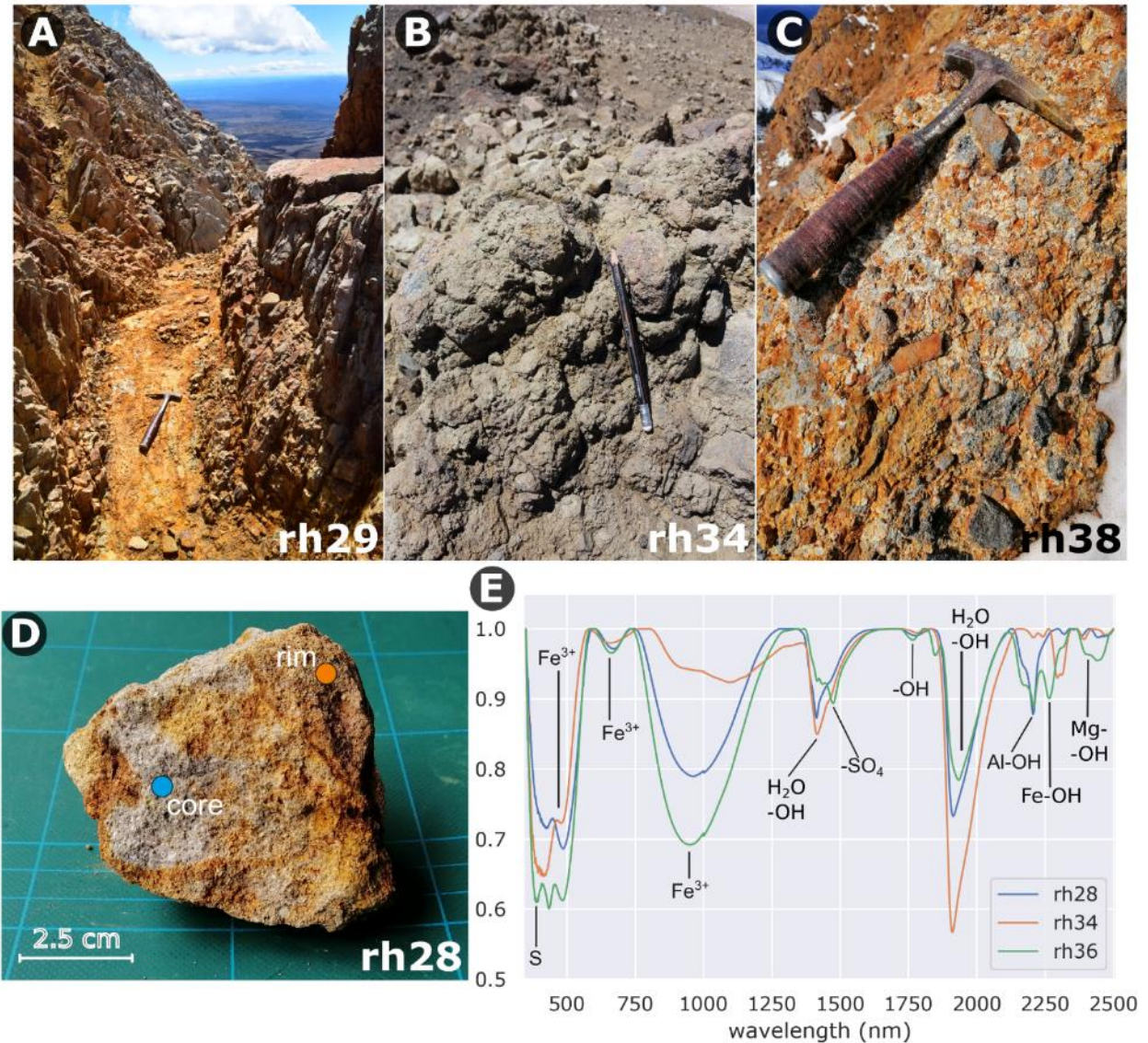
412

#### 413 4.1.3. Intermediate Argillic Alteration

414

415 This group is characterized by brownish to yellowish discoloration, with a partial to full  
416 replacement of the primary rock textures (Figs 4A-C), as well as the development of pervasive  
417 alteration rims with distinct spectral reflectance (Figs 4D-E). These rocks have absorption around  
418 380, 435, 490, 960, 1420, 1780, 1915, 2205, 2290, 2315, 2390, 2480 nm with  $\pm 650$ ,  $\pm 2240$ ,  $\pm 1100$   
419 nm (rh3, rh12, rh26-rh34, rh36-41). The presence of absorption features at 380, 430 and 480 nm  
420 with occasional  $\sim 650$  nm and  $\sim 940$  nm are due to  $\text{Fe}^{3+}$  oxidation (Hunt and Ashley, 1979),  
421 indicating goethite as the main mineral phase with occasional jarosite, schwertmannite and  
422 pyrrhotite (Fig. 4E). These samples lack hematite, indicating formation under acidic conditions  
423 (Schwertmann and Murad, 1983). The SEM-EDS data further indicate that the groundmass of  
424 many alteration samples has disseminated subhedral pyrite with diameters between 5-30  $\mu\text{m}$  (e.g.  
425 rh28, rh36, rh38, rh40, Figs 5A-D). Larger 300-500  $\mu\text{m}$ , euhedral pyrite crystals are also present  
426 occasionally along grain boundaries, and within cavities and fractures (e.g. rh38; Fig. 5D). In  
427 addition to pyrite, Fe-rich, S-poor, occasionally Mn-rich, mineral phases have been identified,  
428 infilling cavity walls and fractures showing colloform, globular and botryoidal morphologies (Fig.  
429 5A), is consistent with Fe-oxides (e.g. goethite), and Fe-sulfates [e.g. schwertmannite  
430 ( $\text{Fe}_{16}\text{O}_{16}(\text{SO}_4)_{12-13} \cdot 10-12\text{H}_2\text{O}$ )]. Jarosite occasionally appears as a pseudomorph after pyrite (e.g.  
431 rh36; Fig. 5C). The paragenesis of this phase is interpreted to be after supergene oxidation of the  
432 sulfide-rich host rock under strongly acidic conditions (e.g. Nordstrom, 1982). The SEM-EDS  
433 results show a higher volume% of pyrite in the Wahianoa than Te Herenga Formation. This can  
434 indicate time differences since those deposits are exposed to atmospheric conditions.

435



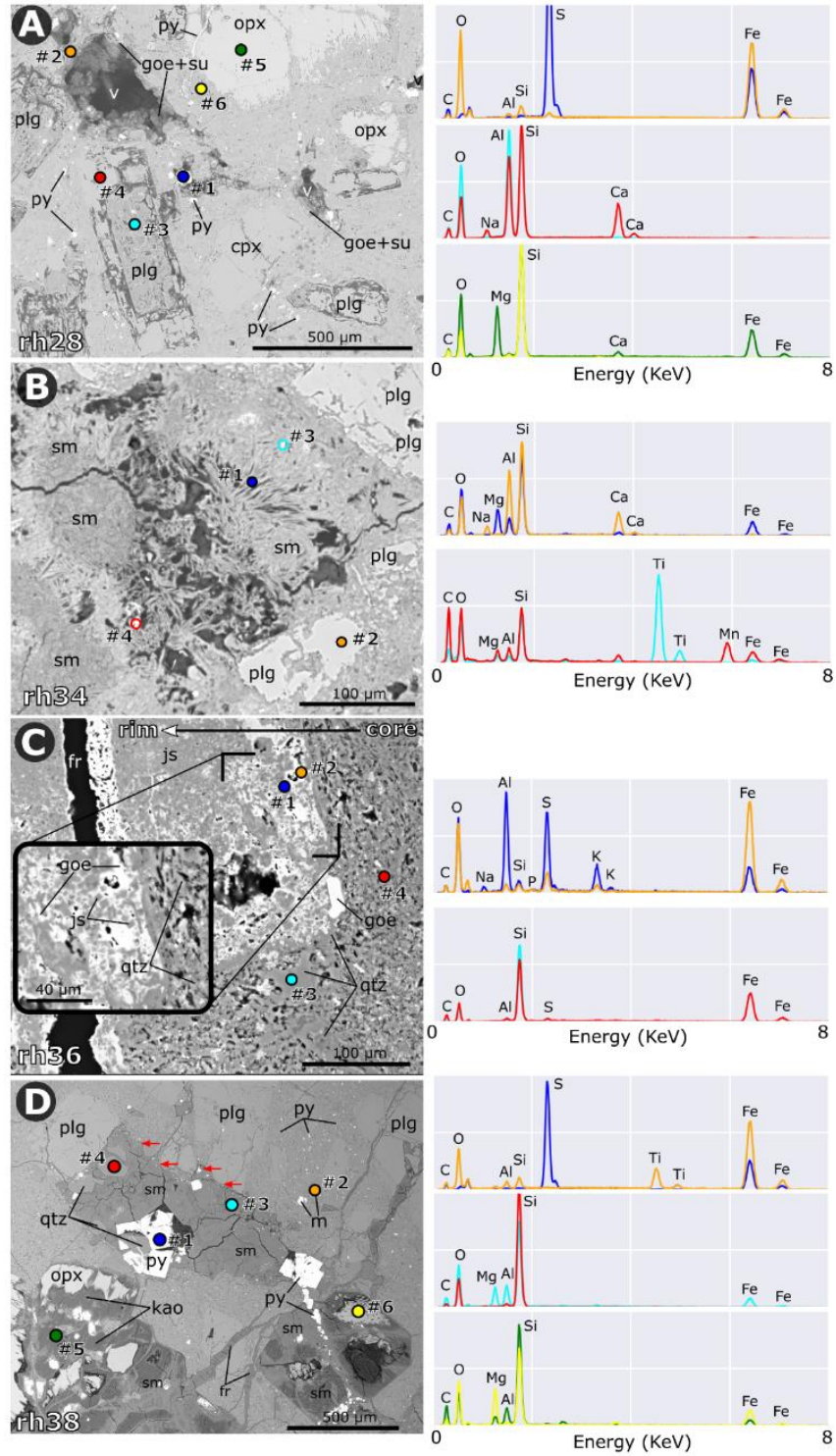
436  
437

438 **Figure 4.** (A-C) Field photos of typical to intermediate argillic alteration on Mt Ruapehu. The  
439 samples are typically moderately to pervasively altered, showing various discoloration and clay  
440 mineral abundances. (D) Sample rh28 shows pervasive alteration preventing a clear distinction  
441 between crystal's rim and core. (E) Spectral reflectance profiles of representative samples. The  
442 spectral reflectance curves show absorption feature SWIR related to atomic vibration between  
443 Al-OH, Fe-OH and Mg-OH bonds, indicating the presence of phyllosilicates.

444

445 Based on SEM-EDS data, both primary plagioclase and pyroxene phases alter to amorphous  
446 Si-rich phases, consistent with various polymorphs of quartz. The alteration leaves abundant rim  
447 and core dissolution structures with well-developed microfractures, occasionally colloform and  
448 pseudomorph crystal habits within cavities (Fig. 5A). These are consistent with acid-induced  
449 mineral dissolution structures (e.g. Farquharson et al., 2019). Ti-magnetite phenocrysts and micro-  
450 phenocryst show commonly trellis-type lamellae textures, indicating leaching of the Fe and  
451 enrichment of Ti-oxides and silicates (e.g. rutile – TiSO<sub>2</sub>, titanite – CaTiSiO<sub>5</sub>), which is in

452 association with pyrite formation. This alteration process is responsible for the decrease of  
 453 magnetic susceptibility of this group, which is between 0 and 0.01 SI (Miller et al., 2020b).  
 454



455  
 456

457 **Figure 5.** SEM (left column) and EDS (right column) results from the representative samples  
 458 intermediate argillic alteration on Mt Ruapehu. The labelled EDS spots are color-coded. (A) rh28  
 459 shows typical phenocryst and micro-phenocrysts dissolution textures and extensive vug  
 460 development with Fe-rich and S-poor infilling, comprising of Fe-oxides and Fe-hydroxy-sulfates.  
 461 This sample is representative for the base of the Pinnacle Ridge. (B) rh34 shows vermiform,  
 462 fibrous and tubular morphologies of smectite-group mineral, occupying fracture and vugs. (C)  
 463 rh36 shows jarosite and goethite developed pseudomorphs after cubic pyrite. The groundmass is  
 464 extensively replaced by silica (qtz). (D) rh38 shows well-developed cubic pyrite crystals co-  
 465 occur with kaolin and smectite-group clay minerals (e.g. #5 and #6 on EDS) occupying vugs  
 466 developed in former phenocrysts. A smaller population of pyrite occupies the interior walls of  
 467 former phenocrysts, shown by red arrows. Abbreviations: v – void/vug, fr – fracture, plg –  
 468 plagioclase, opx – orthopyroxene, cpx – clinopyroxene, m – titanomagnetite, sm – smectites, js –  
 469 jarosite, kao – kaolinite, qtz – quartz, goe – goethite, su – Fe-sulfates, py – pyrite.

470  
 471 The absorption positions at 1420-1430, 1780, 2205, 2290, 2315, 2390 nm are consistent with  
 472 the abundance of Na-Mg-Ca-Fe-rich phyllosilicates, including both kaolin and smectite group  
 473 minerals. The distinction within phyllosilicates is challenging; however, reflectance spectroscopy  
 474 in the VNIR and SWIR can detect vibrational and overtone-derived absorption features with  
 475 hydrous minerals (Hunt and Ashley, 1979). This study used the shape, asymmetry and position of  
 476 the absorption features to discriminate phyllosilicates and sulfates mostly in the SWIR (e.g. Table  
 477 S2). Typically, samples with 1415 and 2205 nm (doublet) feature with inclination/asymmetry  
 478 towards short-wavelength were interpreted as kaolin-group (e.g. kaolinite and halloysite -  
 479  $\text{Al}_2(\text{Si}_2\text{O}_5)(\text{OH})_4$ ). Absorption at 1415, 2205 nm and typically at 2290-2310 nm with  
 480 inclination/asymmetry towards the long wavelength indicated the presence of the smectite group.  
 481 The smectite group mineral were further discriminated by the position of their absorption feature  
 482 at the SWIR region: montmorillonite  $[(\text{Na,Ca})_{0.33}(\text{Al,Mg})_2(\text{Si}_4\text{O}_{10})(\text{OH})_2 \text{ nH}_2\text{O}]$ , nontronite  
 483  $[(\text{Na}_{0.3}\text{Fe}_2((\text{Si,Al})_4\text{O}_{10})(\text{OH})_2 \text{ nH}_2\text{O})]$ , and vermiculite  $[\text{Mg}_{0.7}(\text{Mg,Fe,Al})_6(\text{Si,Al})_8\text{O}_{20}(\text{OH})_4 \text{ 8H}_2\text{O}]$ .

484 The presence of phyllosilicates is often as fracture infilling minerals, showing thin  
 485 crystallites with a vermiform, fibrous and tubular morphologies with hollow interiors, with Mg  
 486 and Fe-enrichment (e.g. Fig. 5B). These textural and morphological features also indicate smectite  
 487 group minerals (Beauchamps et al., 2019; Ece et al., 1999; Ta et al., 2017), indicating the  
 488 dominance of montmorillonite and nontronite. Some samples (e.g. rh26) contains zeolite group  
 489 minerals with acicular and radial crystal habits, occurring in fractures and cavity infilling.

490 Occasionally, euhedral to subhedral, hexagonal to prismatic, disseminated Cl-rich apatite  
 491 crystals ( $\text{Ca}_5(\text{PO}_4)_3\text{Cl}$ ) with diameters ranging from 30 to 50  $\mu\text{m}$ , are embedded in phyllosilicate  
 492 dominated fracture infills. Apatite is a minor, but ubiquitous mineral of plutonic and volcanic  
 493 systems (Piccoli and Candela, 2002), and it is also present on Mt Ruapehu (Price et al., 2012).  
 494 Constraining the paragenesis of this phase is problematic using spectroscopy, optical microscopy  
 495 and SEM-EDS analysis, and it requires cathodoluminescence (Bouzari et al., 2016). The apatite  
 496 found in rh34 contains a minor amount of S and Si, which can be incorporated into the apatite's  
 497 crystal structure (e.g. Streck and Dilles, 1998), potentially indicating its magmatic origin.

498 Aluminum-Phosphate-Sulfate (APS) minerals occur in cavities as well-developed acicular  
 499 crystals and are only observed in samples from the Wahianoa Formation. The SEM-EDS spectra  
 500 show Ca-rich with minor peaks of Al and S, which might correspond to woodhouseite,  
 501  $\text{CaAl}_3(\text{PO}_4,\text{SO}_4)(\text{OH})_6$  (Dill, 2001; Stoffregen and Alpers, 1987). These APS minerals  
 502 occasionally compliment acid-sulfate alteration in high-sulfidation epithermal systems which are

503 rich in Ca, P, Al, dissolved from primary apatite and plagioclase phases (Imura et al., 2019;  
504 Stoffregen and Alpers, 1987).

505 The mineral associations, their spectral, chemical and textural characteristics are all  
506 consistent with intermediate argillic alteration, formed in a highly acidic environment by  
507 hydrothermal fluids with temperatures between 150-250 °C (John et al., 2019; Simmons et al.,  
508 2005). This resulted in abundant pyrite as an oxidation product of the ascending H<sub>2</sub>S-rich fluids  
509 below and around the paleo water table within the proto-Ruapehu edifice, within the Te Herenga  
510 and Wahianoa Formations. The pyrite-bearing rocks were then subject to supergene alteration after  
511 exposure to the atmospheric condition following flank collapses (Palmer and Neall, 1989; Tost et  
512 al., 2015) and erosion (e.g. glaciation and fluvial activity). This led to the formation of smectite-  
513 group minerals, such as montmorillonite and nontronite, and Fe-sulfates, potentially  
514 schwertmannite, both filling in fractures and vugs. Smectite group minerals often form after the  
515 initial oxidation of pyrite, producing acid water, followed by hydrolysis of feldspar and acid water  
516 buffering by the host rock, and colloidal deposition in open cavities and fractures at low-  
517 temperature ( $\leq 40$  °C) (Fernández-Caliani et al., 2004). This paragenesis often produces minor  
518 barite (BaSO<sub>4</sub>) phase (Fernández-Caliani et al., 2004), which has been identified as a minor phase  
519 in XRD (Mordensky et al., 2019a).

520

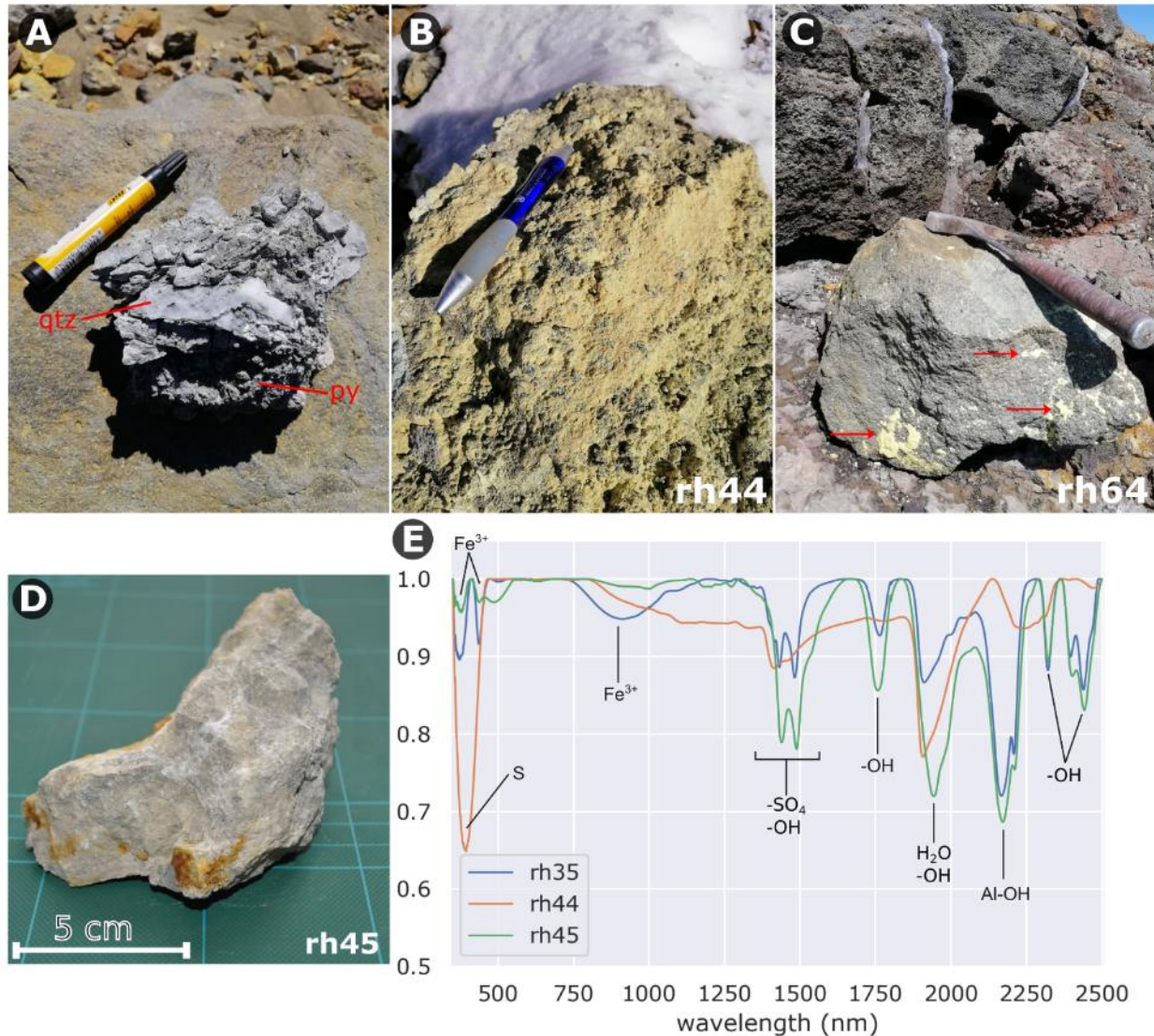
#### 521 4.1.4. Advanced Argillic Alteration with minor silicification

522

523 Advanced argillic alteration occurs in vertical cliffs, and as reworked volcanoclastics deposits  
524 along the upper Whangaehu Valley, around the present-day Crater Lake area, and sampled as  
525 ballistic blocks from past eruptions (Figs 6A-C). These samples are often characterized by white,  
526 grey to pale yellow colors with abundance native sulfur, gypsum, amorphous silica precipitation  
527 and pyrite crystals with diameters up to 2 mm (Figs 6A-D). This group shows typical VNIR-SWIR  
528 absorption features around 380, 430, 480, 940, 1412, 1920, 2170, 2205, 2450 nm with  $\pm 390$ ,  
529  $\pm 1430$ ,  $\pm 1475$ ,  $\pm 1490$ ,  $\pm 1783$ ,  $\pm 2240$ ,  $\pm 2260$ ,  $\pm 2320$ ,  $\pm 2400$  nm (Fig. 6E). The spectral absorption  
530 position is consistent with goethite, phyllosilicates with the dominance of kaolin- group minerals  
531 over the smectite group, native sulfur, sulfates and sulfides. The SEM imagery shows completely  
532 dissolved phenocrysts and micro-phenocrysts of all primary minerals (e.g. Fig. 7A) The  
533 groundmass is often completely replaced by amorphous quartz (e.g. with localized silicification;  
534 Figs 6A and 7). Occasionally, samples show intense local silicification with complete to partial  
535 replacement of groundmass and phenocrysts, accompanied by minor sulfur and barite precipitation  
536 (e.g. blocks from the shore of the Crater Lake – rh52). The Ti-magnetite phases of the primary  
537 volcanic rocks have been completely altered, leaving Ti-rich residue and abundant pyrite crystals  
538 forming euhedral to subhedral on the outside of former magnetite crystals, and disseminated as a  
539 groundmass (Figs 7A and C). The destruction of magnetite produces very low magnetic  
540 susceptibility (e.g. 0 to 0.001 SI).

541 The groundmass occasionally has stockwork textures and colloform banding with vein and  
542 veinlets filled by native sulfur (e.g. rh44; Fig. 7B) and anhydrite (e.g. rh45; Fig. 7C). Anhydrite  
543 (CaSO<sub>4</sub>) can be formed by progressive removal of acid anion species, such as SO<sub>4</sub>, from the  
544 hydrothermal fluids, or by the exchange of aqueous H<sup>+</sup> with cations in the host rock (Smith et al.,  
545 2017; Zimbelman et al., 2005). This paragenesis can also result in precipitation of kaolinite (Hynek  
546 et al., 2013). Samples exposed on the surface for an extended period were subject to depletion of  
547 their sulfur content (e.g. rh12) and hydration processes, forming gypsum, CaSO<sub>4</sub>·2H<sub>2</sub>O (e.g. rh48).

548



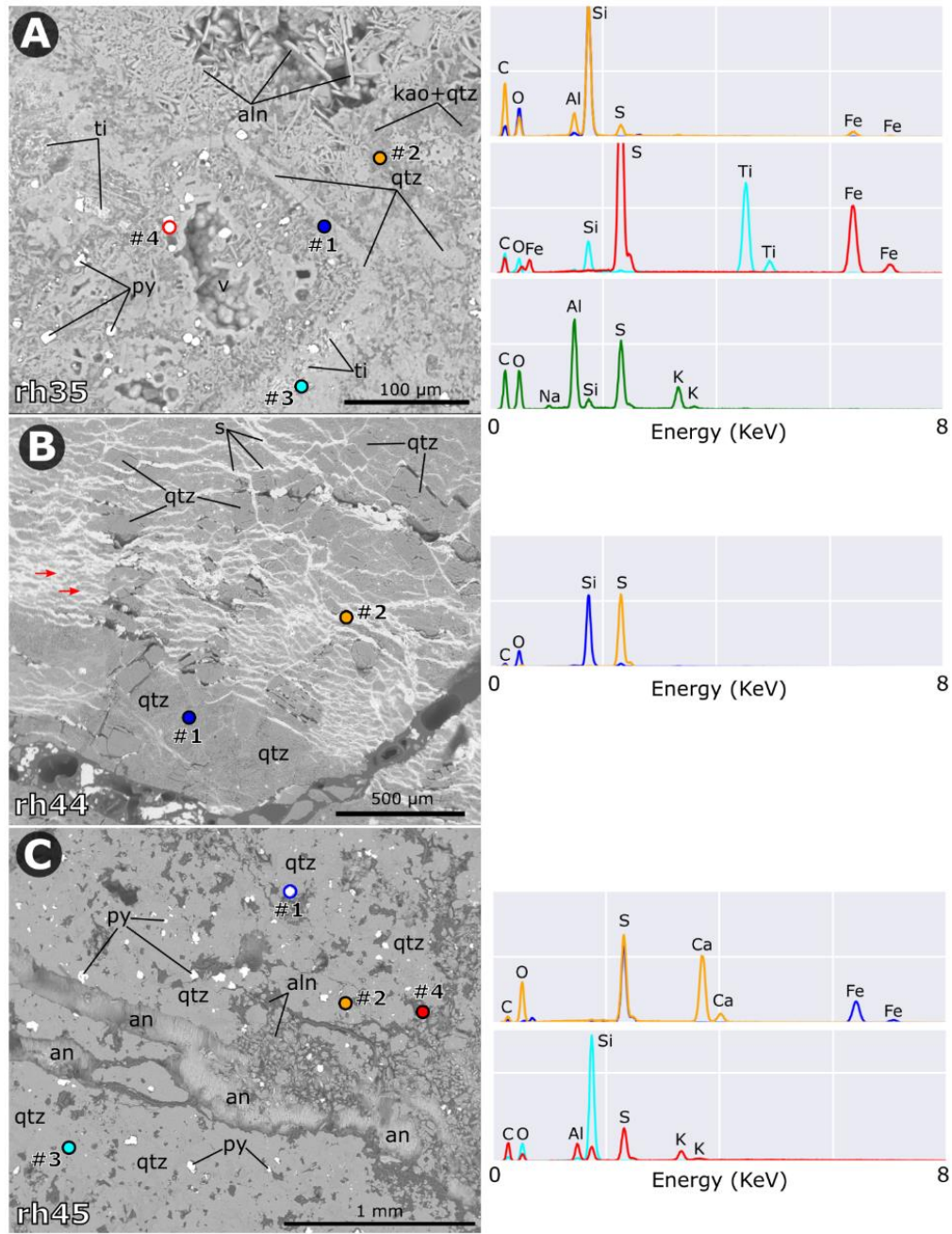
549  
550

551 **Figure 6.** (A-D) Hand specimen samples of the advanced argillic alteration on Mt Ruapehu. The  
552 samples are often disintegrated, white to yellow in color, and show visible precipitation of  
553 pyrite/marcasite and native sulfur. (E) Spectral reflectance profiles of representative samples.  
554 The spectral reflectance curves show typical absorption features at around 1400-1500 nm which  
555 is associated with sulfates (-SO<sub>4</sub>), while strong absorption due to Al-OH bonds and presence of  
556 crystalline water, indicating alunite and phyllosilicates (e.g. kaolin group minerals)

557

558 Besides anhydrite and gypsum, this group has alunite (KAl<sub>3</sub>(SO<sub>4</sub>)<sub>2</sub>(OH)<sub>6</sub>). Alunite exhibits  
559 spectral absorption features (e.g. Fig. 6E) due to the vibrations of hydroxyl (-OH) and metal-  
560 oxygen bonds (Al-OH) and lattice vibrations (Bishop and Murad, 2005). The alunite occurs on Mt  
561 Ruapehu as tabular crystals and as a constituent of the groundmass (Figs 7A and C). Both  
562 reflectance and SEM-EDS data indicate that alunite on Mt Ruapehu is not a pure endmember, but  
563 they show both K and Na enrichments. The origin of alunite is due to the oxidation of acidic fluids  
564 (e.g. H<sub>2</sub>S) between the groundwater table and the surface (Zimelman et al., 2005), or as supergene  
565 alteration of sulfides (Bladh, 1982). Currently, there is no active hydrothermal manifestation (e.g.

566 fumaroles, hot springs) besides the vent-hosted hydrothermal system beneath Crater Lake. The  
 567 current Crater Lake and its hydrothermal system precipitate Na-alunite as oxidation of ascending  
 568 H<sub>2</sub>S hydrothermal fluids (Christenson and Wood, 1993). The formation of alunite within the  
 569 Wahiana Formation is interpreted to be formed under hypogene conditions due to its current  
 570 stratigraphic position (e.g. exposed only at the lower parts of the Whangaehu valley). However,  
 571 further isotope and radiometric dating are needed to confirm its relationship with the currently  
 572 active hydrothermal system under the Crater Lake area.  
 573



574

575

576 **Figure 7.** SEM (left column) and EDS (right column) results from the representative samples  
 577 advanced argillic alteration on Mt Ruapehu. The labelled EDS spots are color coded. (A) rh35

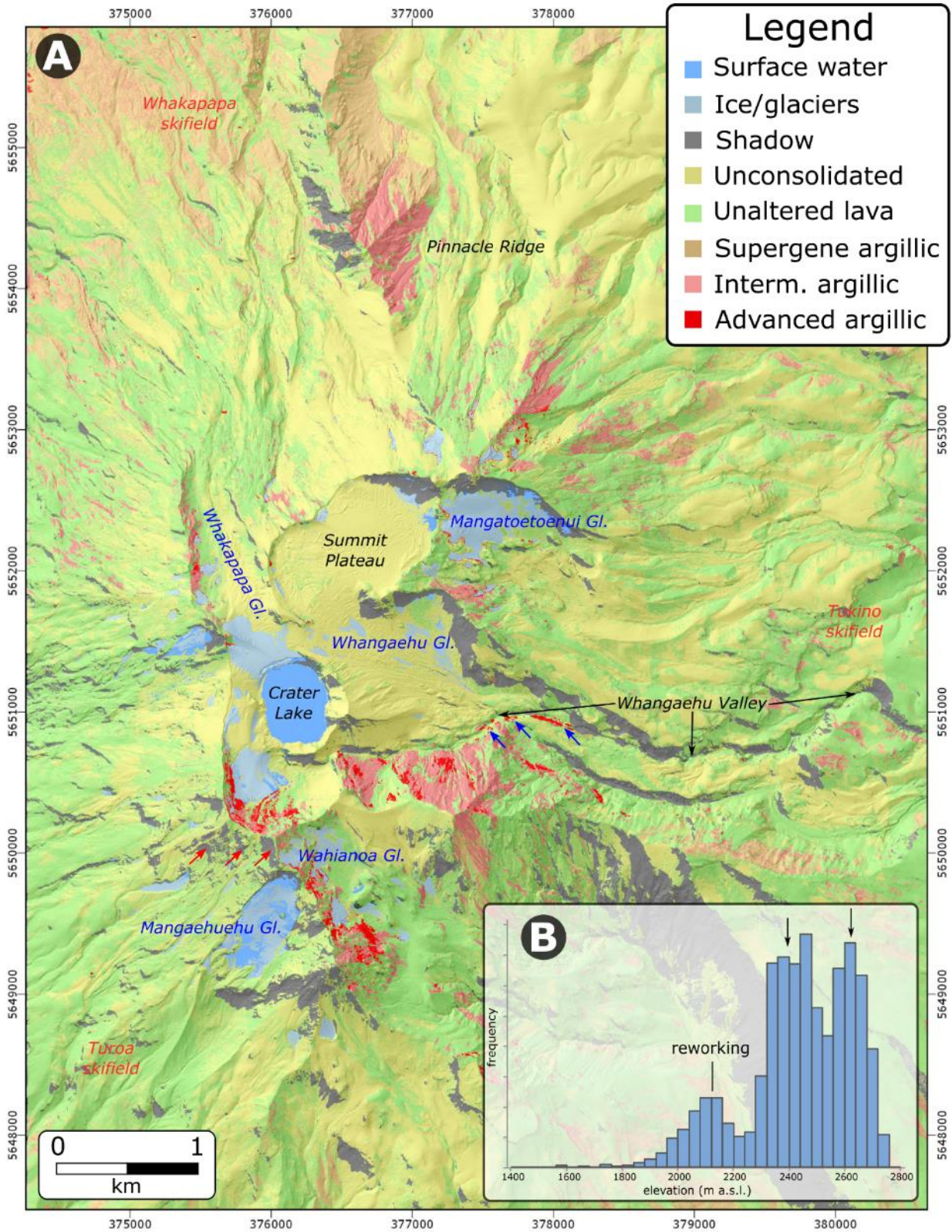
578 shows tabular crystals of alunite, occurring together with kaolinite, pyrite and quartz. The  
579 groundmass and phenocryst are completely replaced by the alteration mineralogy; however,  
580 scattered Ti-rich phases are residues after the primary Ti-rich magnetite population (ti). (B) rh44  
581 show extensive veinlets of precipitated native sulfur. (C) rh45 shows anhydrite filled fracture  
582 surrounded disseminated pyrite, alunite and quartz. Abbreviations: v – void/vug, kao – kaolinite,  
583 qtz – quartz, py – pyrite, al – alunite, s – sulfur, ti – Ti-rich phase.

584  
585 The mineral associations are consistent with advanced argillic alteration (e.g. Sillitoe and  
586 Hedenquist, 2003) formed from a low pH of 1-4, hot hydrothermal fluids (120-300 °C), circulating  
587 within a magmatic-hydrothermal system (Boyce et al., 2007; John et al., 2019; John et al., 2008;  
588 Simmons et al., 2005; Swayze et al., 2014). However, the hydrothermal alteration can change on  
589 a small-scale between advanced argillic and intermediate argillic alteration styles.

#### 590 591 4.2. Surface Mapping using Hyperspectral Imaging

592  
593 The airborne hyperspectral image was used to create a hydrothermal alteration map of Mt  
594 Ruapehu through supervised image classification using a Random Forest algorithm (Fig. 8). The  
595 training process for the image classification was guided by the hydrothermal alteration mineralogy  
596 from SEM-EDS and spectroscopy analysis. The image classification accuracy using an  
597 independent validation population is 92.6%. Full retrieval of alteration classification on the surface  
598 is affected by the heavy cover of tephra, snow and ice on the surface of Mt Ruapehu (35.7% of the  
599 total area; Table 1) and the presence of shadows (Fig. 8A). The second largest unit mapped is the  
600 unaltered lava rocks (22.8 km<sup>2</sup>). Supergene, intermediate and advanced argillic alteration have  
601 much smaller spatial extent on the surface, composing 4.8 km<sup>2</sup>, 2.4 km<sup>2</sup> and 0.2 km<sup>2</sup> of the total  
602 area, respectively (Table 2). Accounting for the extensive surface cover, these hydrothermal  
603 alteration zones are expected to be minimum figures. The spectral average of the input training  
604 data shows distinct differences, including spectral features at 405, 493, 670 and 995 nm (goethite,  
605 hematite), 1160 nm (smectites), 1430-1495 nm (kaolinite, alunite, jarosite), 1763 nm (alunite),  
606 2174 nm (alunite), 2200-2210 (Al-rich phyllosilicates), 2265 nm (jarosite), 2300-2390 nm (Fe-  
607 and Mg-rich phyllosilicates) (Fig. 9). These indicate that those minerals are critical to spectrally  
608 separate the mapped hydrothermal alteration types using airborne hyperspectral imagery.

609

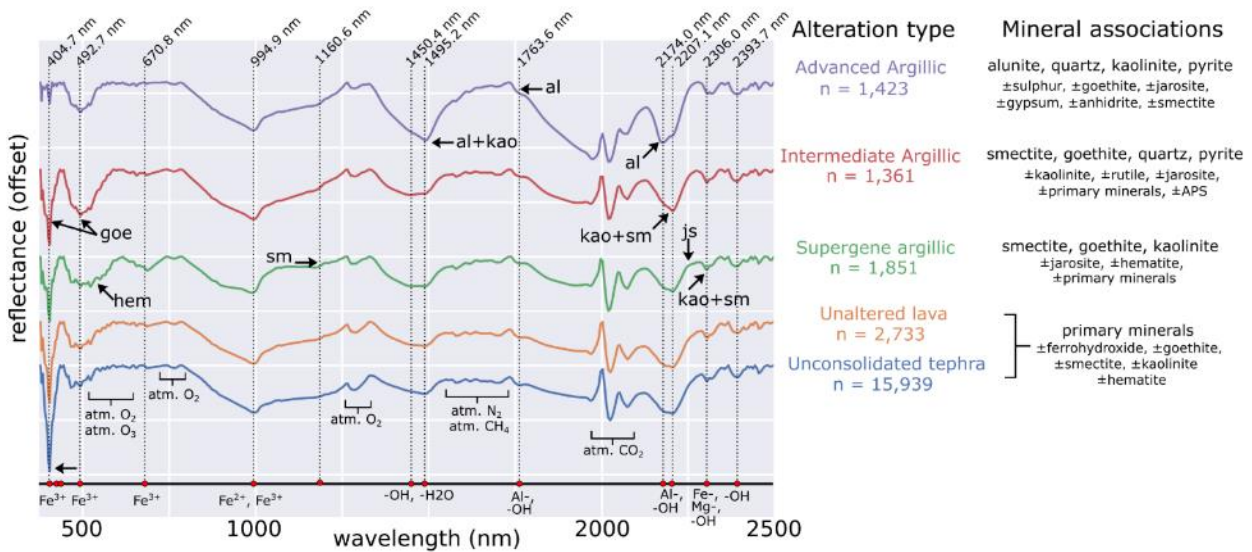


610  
611  
612  
613

**Figure 8.** Hydrothermal alteration map of Mt Ruapehu based on the airborne hyperspectral imagery (A). The blue arrows show the location of the reworked deposits of the advanced argillic

614 alteration (e.g. samples rh44, rh45) along the Upper Whangaehu valley. Red arrows indicate  
 615 areas with outcropping intermediate alteration (e.g. rh36), misclassified as shadow. The inset (B)  
 616 shows the elevation histogram of the advanced argillic alteration rocks mapped by hyperspectral  
 617 imaging, showing they occur predominantly at two distinct elevations (black arrows).  
 618

619 The error matrix shows numerous misclassifications between unconsolidated tephra and  
 620 unaltered lava rocks (Table 1). This can be due to the similar chemical composition, resulting in  
 621 similar reflectance profiles. Therefore, the spectral discrimination is most likely due to overall  
 622 intensity of the reflected light, which, in turn, is a function of the grain size and illumination  
 623 geometry (e.g. Clark and Roush, 1984). Another misclassification occurs between the supergene  
 624 argillic and the intermediate argillic alteration types (Table 1). However, this misclassification  
 625 occurred less frequently due to the presence of an absorption feature at 671 nm (e.g. goethite,  
 626 ferrihydrite and hematite).  
 627



628  
 629  
 630 **Figure 9:** Continuum-removed spectral reflectance curves for the alteration classes on Mt  
 631 Ruapehu, showing spectrally distinct absorption features of each class and the inferred  
 632 mineralogy (black arrows) due to their unique mineralogy (right column). The graph also  
 633 indicates the location of the atmospheric gasses, manifesting as noise in the hyperspectral data.  
 634 The spectral curves are offset for clarity. Abbreviations: kao – kaolinite, al – alunite, sm –  
 635 smectites, js – jarosite, goe – goethite, hem – hematite.  
 636

637 The most spectrally distinct class is the advanced argillic, due to its unique and pronounced  
 638 absorption located at 2174 nm (alunite) and 2205 nm (kaolinite) (Fig. 9). The mapped occurrences  
 639 correspond to three distinct elevation regions (Fig. 8B): (1) The lower occurrences correspond to  
 640 the reworked deposits, along with the Whangaehu valley (blue arrows in Fig. 8A). The other two  
 641 populations can indicate a spatial and temporal difference between the formation of advanced  
 642 argillic suites (e.g. Wahianoa Formation versus the current Crater Lake hydrothermal system).  
 643

644 **Table 1:** Error matrix of the supervised image classification using the independent validation  
 645 data (vertical columns) against the image classification results (horizontal rows). The values are  
 646 pixel numbers. The highlighted values highlight the misclassifications.  
 647

		Image class								
Validation class	classes	water	ice	shade	tephra	unaltered lava	supergene argillic	intermediate argillic	advanced argillic	Total
	water	<b>3,381</b>	132	44	0	0	0	0	0	3,557
	ice	0	<b>1,952</b>	0	0	0	0	0	0	1,952
	shade	0	0	<b>5,820</b>	4	0	0	0	0	5,824
	tephra	2	0	0	<b>15,599</b>	699	9	3	18	16,330
	unaltered lava	5	0	0	1,094	<b>1,819</b>	77	69	0	3,064
	supergene argillic	0	0	0	47	26	<b>1,203</b>	42	0	1,318
	intermediate argillic	0	0	0	0	68	148	<b>727</b>	2	945
	advanced argillic	0	0	0	0	0	0	3	<b>595</b>	598
	Total	3,388	2,084	5,864	16,744	2,612	1,437	844	615	33,588

648 **Table 2:** Area statistics and image classification accuracy by image classes and hydrothermal  
 649 alteration types on Mt Ruapehu.  
 650

651

Classes	Alteration type/surface feature	User's Accuracy [%]	Producer's Accuracy [%]	Total area [pixel]	Total area [km <sup>2</sup> ]
class 1	surface water	95.05	99.79	202,329	0.46
class 2	glaciers/snow	100	93.67	402,495	0.91
class 3	shadow	99.93	99.25	1,420,459	3.20
class 4	unconsolidated tephra	95.52	93.16	8,601,991	19.35
class 5	non-altered lava	59.37	69.64	10,158,097	22.86
class 6	supergene argillic alteration	91.27	83.72	2,125,567	4.78
class 7	intermediate argillic alteration	76.93	86.14	1,075,363	2.42
class 8	advanced argillic alteration	99.5	96.75	93,699	0.21

652

653

654

655

656

## 4.3. Subsurface Mapping using Aeromagnetic Data

The 3D depth of hydrothermal alteration can be mapped using aeromagnetic data and subsequent inversion models (Finn et al., 2018; Finn et al., 2001; Miller et al., 2020b), if the lack of the magnetic susceptibility is due to hydrothermal alteration which dissolves (Ti-) magnetite crystals. Based on the SEM imaging, there is a systematic dissolution of (Ti-) magnetite with increasingly pervasive hydrothermal alteration (Fig 10). Therefore the magnetic susceptibility measurements and the inversion model of Mt Ruapehu (Miller et al., 2020b) indicates the hydrothermal alteration, which can be used to link surface alteration patterns from the hyperspectral image classification (Figs 10D and 11). However, identifying low magnetic susceptibility caused by hydrothermal alteration is complicated by the variable amounts of magnetite content and its Ti-impurity in the host rock (Fig. 10D), meaning that some fresh, low magnetite content andesites can have similar magnetic susceptibility to supergene alteration. Intermediate and advanced argillic alteration deposits tend to have, however, generally lower magnetic susceptibility (e.g.  $\leq 0.01$  SI; Fig 10D).

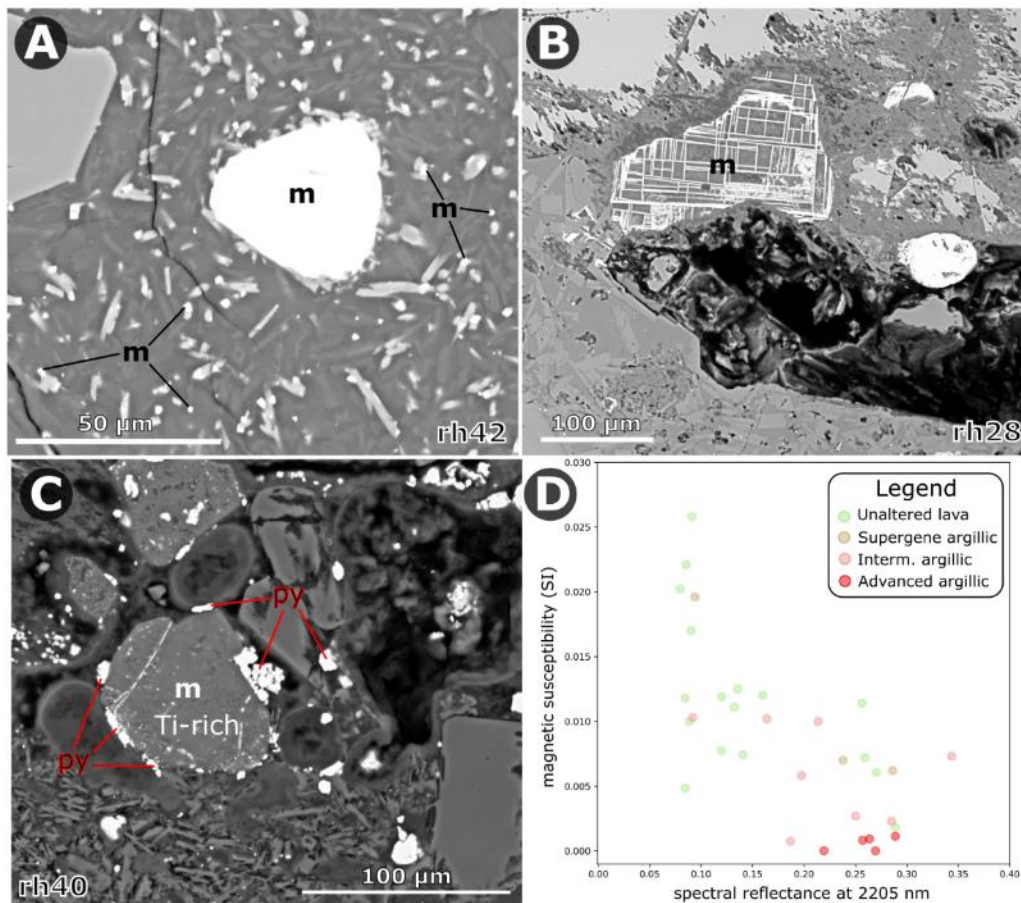
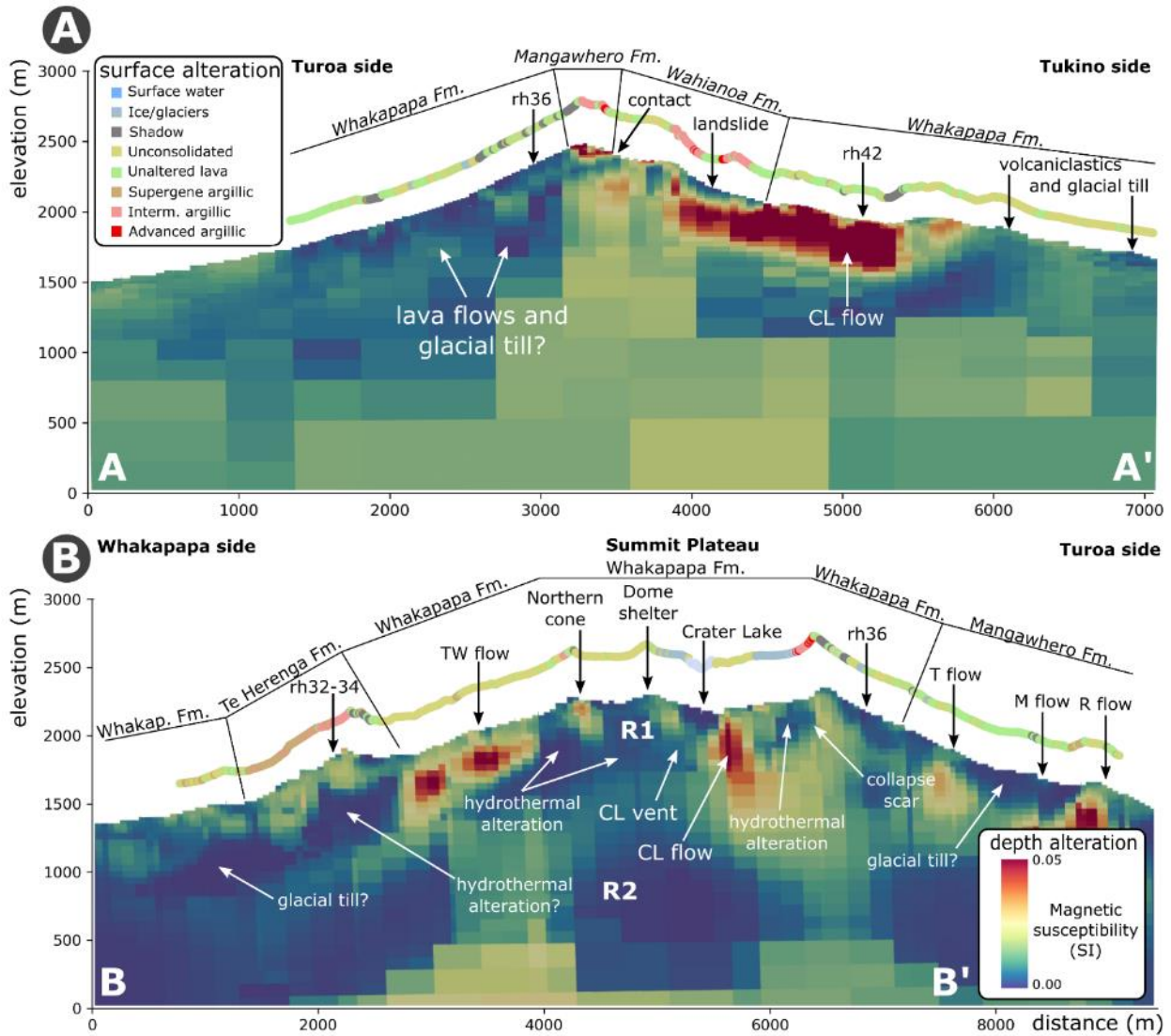


**Figure 10.** Titanomagnetite dissolution textures as a function of hydrothermal alteration types: (A) non-altered, (B) intermediate with well-developed trellis structures, and (C) advanced argillic alterations. (D) The graph shows the relationship between measured magnetic susceptibility values (SI) and spectral reflectance at 2205 nm.

680 The largest region of hydrothermally altered rocks is located within the Pinnacle Ridge on  
681 the southeastern flanks and to a moderate extent beneath the entire Summit Plateau. The cross-  
682 cutting dykes exposed at the Te Herenga Formation show higher magnetic susceptibility compared  
683 to the lavas of the Wahianoa Formation, possibly due to the larger grain size of the intruded rocks.  
684 The low to moderate levels of magnetic susceptibility (e.g. Turoa side; Fig. 11) are due to  
685 volcanoclastic deposits, mixed with glacial sediments and thin intercalated lava flows (Conway et  
686 al., 2016; Townsend et al., 2017), which some of might also be hydrothermally altered (Miller et  
687 al., 2020b). The demagnetized zones beneath Summit Plateau are patchy (Fig. 11B), in agreement  
688 with electrical resistivity highs observed in the magnetotelluric model, which suggest the  
689 dominance of chlorite (Jones et al., 2008). The geophysical model linked with alteration  
690 mineralogy and surface alteration distribution from the hyperspectral imaging indicates that the  
691 hydrothermal alteration interpreted in the aeromagnetic model mostly corresponds to intermediate  
692 argillic alteration. Intermediate argillic alteration is rich in smectite-group minerals, which can  
693 explain the observed the high electrical resistivity zone beneath the northern part of the Summit  
694 Plateau [e.g. “R1” anomaly in Jones et al. (2008)]. Moreover, this alteration type has a wide range  
695 of magnetic susceptibilities (0.001 to 0.01 SI) (e.g. Fig. 10D), contributing to the patch-work  
696 patterns in the aeromagnetic data (Miller et al., 2020b).

697



698  
699

700 **Figure 11.** Cross-section through the magnetic susceptibility model of Mt Ruapehu along the A-  
 701 A' and B-B' profiles from Fig. 1. On (B), R1 and R2 correspond to the electric resistivity highs  
 702 from Jones et al. (2008). The dots above the topography show the hydrothermal alteration types  
 703 mapped on the surface using hyperspectral imaging. The colors correspond to Fig. 11, and the  
 704 profiles are offset by 200 m for clarity. Abbreviations: CL vent – Crater Lake vent; CL flow -  
 705 Crater Lake Member lava of Whakapapa Formation (5-y); TW flow - Iwikau Member of  
 706 Whakapapa Formation - Tawhainui flows (6 ky); T flow - Turoa Member of Whakapapa  
 707 Formation (15-12 ky); M Flow - Mangaehuehu Member of Mangawhero Formation (45-42 ky);  
 708 R flow - Rangataua Member lava of Whakapapa Formation (10-15 ky).

709

710

## 711 5. Discussion

### 712 5.1. Integration of Hyperspectral Imaging with Airborne Geophysics

713

714 Airborne hyperspectral remote sensing can identify hydrothermal alteration minerals, and  
715 through image classification, a hydrothermal alteration map can be created. The hydrothermal  
716 alteration map only represents surface alteration, which can be heavily hampered by the surface  
717 cover (e.g. tephra, glacial till, alluvium and colluvium accumulation). However, the distribution of  
718 the hydrothermal alteration can still be reconstructed with the aid of ancillary field data through  
719 microscopic petrographical and mineralogical information. Hyperspectral imaging provides a  
720 versatile framework for hydrothermal alteration mapping, which correlates well with the magnetic  
721 susceptibility model of Mt Ruapehu (e.g. Fig. 11). Conversely, the inversion of aeromagnetic data  
722 can indicate spatial distribution of subsurface alteration at depth, but it provides no information on  
723 the style of hydrothermal alteration, and interpretation of moderate alteration can be misled by  
724 unaltered rocks with similar magnetic susceptibility. Furthermore, aeromagnetic data is also  
725 insensitive to rock water saturation that is a key determinant in slope stability (Finn et al., 2018;  
726 Miller et al., 2020a). Thus, limitations in both hyperspectral remote sensing and geophysical data  
727 can be overcome by integrating both methods, allowing a comprehensive assessment of both  
728 surface and subsurface alteration patterns.

729 The paragenesis of hydrothermal alteration types and volumes of the altered rock masses  
730 provide a great conceptual model for volcanic hydrothermal systems, vastly improving our  
731 understanding of volcanic evolution and associated natural hazards. Specifically, at Mt Ruapehu,  
732 since the hydrothermal alteration is only exposed along ridge tops and on steep slopes off of these  
733 ridges because of tephra cover, the extent of hydrothermal alteration is seemingly minor on the  
734 surface. However, geophysical data (e.g. aeromagnetic) suggests a much larger extent is altered.  
735 This is likely the case at similar long-lived volcanoes worldwide. This calls for the need to integrate  
736 remote sensing and geophysical datasets for developing new volcano assessment tools to monitor  
737 and map shallow hydrothermal alteration within composite volcanoes.

738 Further direction to utilize hyperspectral remote sensing for hydrothermal alteration  
739 mapping can include mapping of individual mineral species through spectral feature matching  
740 (Clark et al., 2003), or wavelength mapping (van der Meer et al., 2018). Moreover, alteration  
741 minerals often occur as an intimate granular mixture, requiring spectral unmixing algorithms  
742 (Roberts et al., 1998), or using regression approaches with synthetically mixed training data  
743 (Okujeni et al., 2013). These research directions will need dedicated studies in the future.

744

## 745 5.2. The Role of Mineral Imprinting

746

747 The weathering and hydrothermal alteration on Mt Ruapehu has produced diverse mineral  
748 suites, some of which can be formed through multiple paragenesis including supergene  
749 modification through oxidation of sulfides, such as pyrite exposed to groundwater or surface water  
750 (Fig. 12A). These processes cause changes to meta-stable hydrothermal alteration minerals,  
751 leading to “imprinting”, complicating the reconstruction of hydrothermal alteration history on  
752 long-lived composite volcanoes. For example, supergene oxidation can form jarosite (in Fe-rich  
753 low pH conditions), alunite (in moderate pH and Al-rich conditions), as well as hydroxy-sulfate  
754 and oxyhydroxide minerals (Bishop and Murad, 2005; Schwertmann and Murad, 1983; Zolotov  
755 and Shock, 2005), which cannot be discriminated by spectroscopic techniques and hyperspectral  
756 remote sensing. Mt Ruapehu has abundant Fe-oxides, mostly goethite, which can be formed from  
757 both oxidation processes of primary mineral phases rich in Fe (e.g. titanomagnetite, clino- and  
758 orthopyroxenes) and oxidation and breakdown of hydrothermal pyrite (Brady et al., 1986; Noack  
759 et al., 1993). The abundance of goethite, and its confinement to higher flanks, can also be attributed

760 to the extensive glacial history of Mt Ruapehu. The chemical weathering occurring beneath  
761 glaciers is primarily driven by microorganic activity, thriving on meltwater solution rich in  
762 oxidized pyrite, silica and anions, such as  $\text{SO}_4^{2-}$  (Mitchell et al., 2013; Rutledge et al., 2018).

763 The integration of field sampling, hyperspectral and aeromagnetic data have, however,  
764 allowed us to constrain the spatial distribution of inactive and currently active hydrothermal  
765 systems, allowing discrimination of mineral imprinting processes on Mt Ruapehu (Fig. 12B).  
766 These correspond to the oldest Te Herenga Formation, outcropping at the Pinnacle Ridge (Fig. 1,  
767 8), in which the intrusion-related hydrothermal system lead to acid sulfate alteration, causing  
768 primary mineralogy to be altered to pyrite, phyllosilicates, quartz-dominated alteration minerals,  
769 superimposed with extensive smectite formation due to prolong surface oxidation of pyrite (Fig.  
770 12B). This leads to distinct vertical and stratigraphic changes in a sulfide-to-clay ratio within the  
771 altered rocks. Areas <2000 m a.s.l. show less extensive oxidation of pyrite (e.g. rh28) than the  
772 elevated, >2100 m a.s.l parts of the Pinnacle Ridge (rh32-34). This can be explained by the delay  
773 in surface erosion and thus the exposure of the sulfides to atmospheric  $\text{O}_2$ , leading to enrichment  
774 of smectites.

775 The second oldest part of Mt Ruapehu is the Wahianoa Formation that hosts extensive areas  
776 of intermediate argillic alteration (Fig. 12B). The alteration mineralogy and textures (e.g. sharp  
777 boundaries of the pyrite crystals) are better preserved than within the Te Herenga Formation,  
778 indicating much shorter exposure to atmospheric conditions. This observation is in line with the  
779 geological history of the upper Whangaehu valley (Fig. 1 and 8), which developed after the  
780 Mangaio flank collapse 4.6 ky ago (Donoghue and Neall, 2001). Furthermore, the Wahianoa  
781 Formation also hosts advanced argillic alteration (e.g. alunite, pyrite, quartz and phyllosilicates).  
782 This can originate from (1) surface oxidation of pyrite, (2) within the magmatic-hydrothermal  
783 system that existed during the Wahianoa Formation time, or (3) a steam-heated overprinting  
784 alteration due to the proximity of the currently active Crater Lake hydrothermal systems by  
785 condensation of magmatic vapor into the later outflow of groundwater (Fig. 12B). In (2) and (3),  
786 the alunite formed directly due to the ascent-driven oxidation of  $\text{H}_2\text{S}$ -rich fluids and wall-rock  
787 interactions. Alunite, however, occurs with anhydrite on Mt Ruapehu, which is more consistent  
788 with the paragenesis of (2). The distribution of alunite bearing rocks, therefore, can indicate the  
789 position of the paleo water table within the Wahianoa eruptive center between 80-50 ky ago. The  
790 lowest levels of in-situ alunite occurrence on Mt Ruapehu is at 2250 m a.s.l. This elevation is just  
791 slightly higher than the maximum elevation of the Pinnacle Ridge (2237 m a.s.l.), potentially  
792 indicating the role of erosion on the exposure of alunite-bearing rocks.

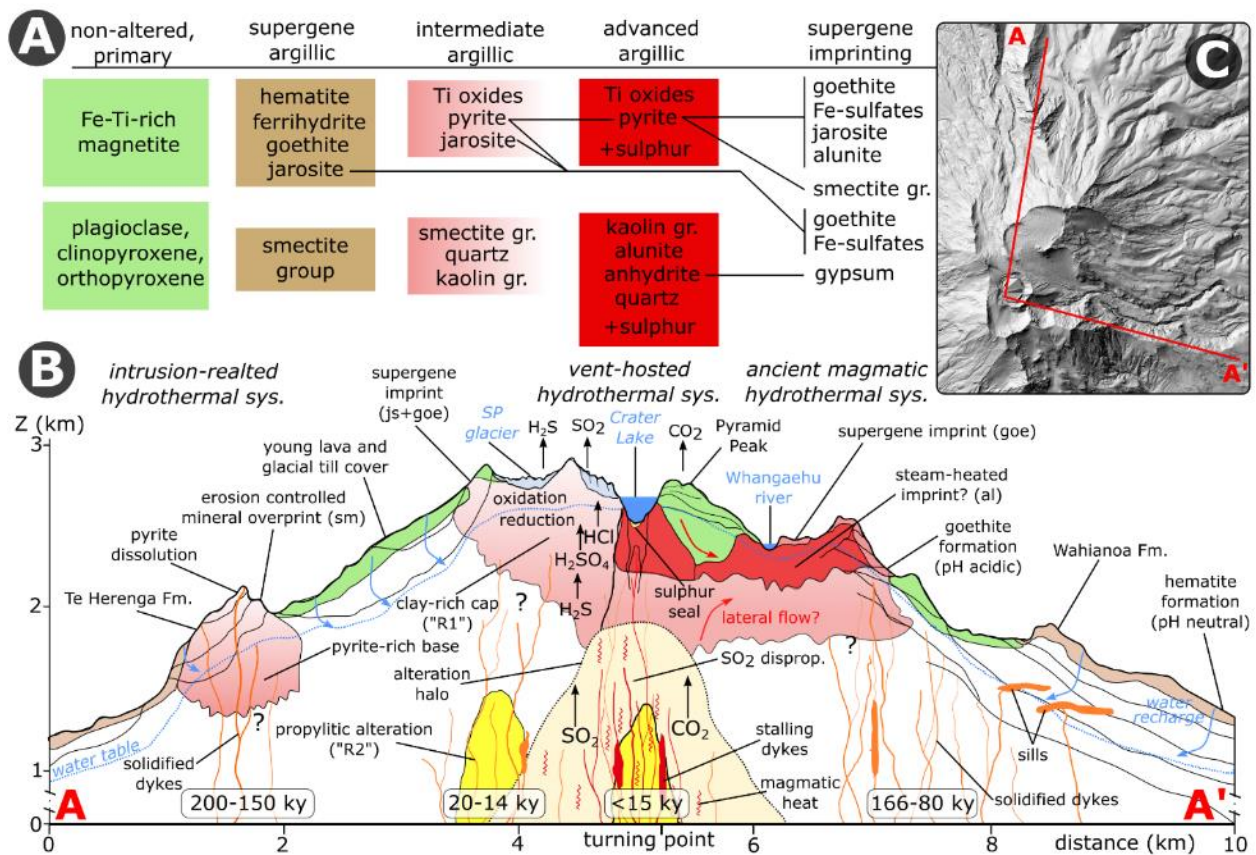
793

### 794 5.3. A Model for Hydrothermal Alteration

795

796 Aeromagnetic data observes that Mt Ruapehu currently has an active but spatially confined  
797 vent-hosted hydrothermal system (Christenson and Wood, 1993). This is in sharp contrast with the  
798 neighboring Tongariro Volcanic Complex, in which has abundant hydrothermal surface  
799 manifestation, including fumaroles and hot pools (Miller et al., 2018; Moore and Brock, 1981).  
800 This observation is in line with the hyperspectral image-derived hydrothermal alteration map,  
801 which does not indicate pervasive hydrothermal alteration across the summit area. While there is  
802 limited surface hydrothermal alteration on Mt Ruapehu (i.e. intermediate and advanced argillic  
803 styles), covering 2.6  $\text{km}^2$  or only 5% of the total area (Fig. 8), the location of this alteration is  
804 scattered throughout the mapped areas. This indicates a complex spatial-temporal evolution of

805 hydrothermal activity at Mt Ruapehu that reflects discrete development stages over the last 200 ky  
 806 (Fig. 12).  
 807



808  
 809  
 810 **Figure 12.** A model for surface weathering and hydrothermal alteration on Mt Ruapehu volcano.  
 811 (A) Hydrothermal alteration sequence of typical primary minerals (green), and their supergene  
 812 argillic (light brown), intermediate (light pink) and advanced (red), their supergene imprinting  
 813 mineral associations. (B) The distribution of hydrothermal alteration types and the main  
 814 hydrothermal features on Mt Ruapehu along the A-A' profile line in (C). Abbreviations: SP  
 815 glacier – Summit Plateau glacier.  
 816

817 At Mt Ruapehu, the source of the magmatic heat and gasses are located at depths between 2  
 818 and 9 km as a network of stalling and crystallizing dykes, forming a melt-rich crystal mush inferred  
 819 from volatile content and major element chemistry of groundmass glass and phenocryst-hosted  
 820 melt inclusions (e.g. Kilgour et al., 2013). This zone has also been imaged as a resistivity anomaly  
 821 in magnetotelluric (Ingham et al., 2009) and seismic tomography surveys (Rowlands et al., 2005).  
 822 This network of magma releases magmatic gasses (e.g. H<sub>2</sub>O, CO<sub>2</sub> and SO<sub>2</sub>; Fig. 12B), which after  
 823 disproportionation can form acidic hydrothermal fluids dominated by H<sub>2</sub>S, and precipitate native  
 824 sulfur (Christenson et al., 2010; Mavrogenes and Blundy, 2017). This type of hydrothermal fluid  
 825 promotes acid sulfate wall-rock alteration within the volcanic edifice above the magmatic heat  
 826 source (Rye et al., 1992; Zimbelman et al., 2005). The low pH hydrothermal fluids then induce  
 827 wall-rock alteration at depth underneath the currently active Crater Lake. A similar ancient

828 hydrothermal system has been imaged by magnetotelluric surveys beneath the northern Summit  
829 Plateau as a vertically elongated high resistivity zone, which can correspond to a chlorite-rich  
830 altered zone (Jones et al., 2008). Chlorite is a typical indicator mineral of propylitic alteration  
831 (Neal et al., 2018). A broader region around this zone also appears to be demagnetized (e.g. Fig.  
832 12B; Miller et al., 2020b), which can correspond to the development of an enlarged alteration halo  
833 (Fig. 12B).

834 Propylitic alteration often grades vertically into intermediate argillic alteration (e.g. John et  
835 al., 2019), which outcrops only sporadically around the Summit Plateau, as indicated by the  
836 hyperspectral remote sensing data (Fig 8). This type of alteration occurs as the ascending H<sub>2</sub>S-rich  
837 hydrothermal fluids react with the andesitic host rock's ferrous minerals (e.g. titanomagnetite) to  
838 form sulfides, such as pyrite, under reducing conditions (e.g. rh38, rh40, rh28, rh33; Fig. 12A), as  
839 observed similarly at Mt Rainer, USA (John et al., 2008). This leads to the formation of  
840 disseminated pyrite crystals. On Mt Ruapehu, well-developed, cubic pyrite crystals are typical,  
841 indicating hydrothermal fluid supersaturation conditions and higher formation temperatures of  
842 ~250 °C (e.g. Murowchick and Barnes, 1987). The dissolution of Ti-magnetite population is also  
843 responsible for demagnetization of the host rock, making it possible to detect hydrothermal  
844 alteration using aeromagnetic techniques (e.g. Fig. 11B; Miller et al., 2020b). This zone has also  
845 been mapped as a higher-resistivity zone on magnetotelluric data (e.g. R1 in Fig. 13B; Jones et al.,  
846 2008), indicating the dominance of intermediate argillic alteration beneath the entire Summit  
847 Plateau (Fig. 12B). This area corresponds to the relict hydrothermal system of the Paretaitonga  
848 and Tureiti cones, active between 20 and 12 ky ago (Townsend et al., 2017). Besides the  
849 precipitation of pyrite, and enrichment of Ti, the wall-rock alteration on Mt Ruapehu also leads to  
850 K and partial Na and Ca depletions, and Si, Al, Fe, Mg and O enrichments, along with the  
851 formation of kaolin and smectite group minerals (Fig. 12A).

852 At locations of intense hydrothermal fluid circulation, the intermediate argillic alteration  
853 transitions into advanced argillic alteration, characterized by the abundance of sulfate minerals  
854 (e.g. alunite), and localized zones of silicification (e.g. vuggy texture). Sulfates (e.g. alunite,  
855 anhydrite and barite) often form around or above the water table within a hydrothermal system due  
856 to oxidation of the ascending H<sub>2</sub>S-rich fluids (Fig. 12B) (Rye, 2005; Zimelman et al., 2005).  
857 These are limited to areas directly beneath the Crater Lake and within the Wahianoa Formation  
858 (Fig.12B). The origin of sulfate precipitation within the Wahianoa Formation can be either (1)  
859 associated with the magmatic-hydrothermal system developed during the Wahianoa Formation, or  
860 (2) formed as a steam-heated alteration on the margin of the currently active Crater Lake  
861 hydrothermal systems due to lateral flow of groundwater (Fig. 12B). The origin can be further  
862 investigated using stable isotope geochemistry and K-Ar radiometric dating on the K-phase within  
863 the alunite.

864

#### 865 5.4. Volcanic Hazard Implications

866

867 The influence of alteration on physical and mechanical rock properties depends on rock type,  
868 initial microstructural and physical properties of the rock, nature of the hydrothermal fluid, and  
869 duration of rock-fluid interaction, resulting in varying processes of mineral dissolution,  
870 replacement, and/or precipitation (Heap et al., 2020 and references therein). This study described  
871 the production of kaolin and smectite phyllosilicate clay minerals as a result of acid-sulfate  
872 alteration. The main consequences of the formation of these clay minerals are the replacement of  
873 strong rock by a weaker, clay-rich rock, precipitation of clay into pores and microfractures, and

874 the deposition of clay along bedding structures or at the interface between volcanic deposits (Heap  
875 et al., 2019; Watters et al., 1995). The degree/intensity of clay alteration combined with the degree  
876 of saturation has been shown to alter overall strength, density, and elasticity of volcanic rock  
877 (Mordensky et al., 2019a; Siratovich et al., 2016; Watters et al., 1995; Wyering et al., 2014).  
878 Experimental observations have also shown that an increase in alteration increases the propensity  
879 for pore collapse or ductile failure behavior (Mordensky et al., 2019a; Siratovich et al., 2016),  
880 which decreases porosity and permeability as the material is deformed and pores are compacted  
881 (e.g. Farquharson et al., 2017). This, in turn, has implications for pore fluid pressure, magma  
882 degassing, and eruption characteristics (Cassidy et al., 2018; Heap et al., 2019; Okumura and  
883 Sasaki, 2014). For example, a reduction in permeability from clay precipitation into pores and  
884 fractures can prevent the migration of hydrothermal fluids or magma degassing, leading to  
885 increased pore pressures that can decrease material strength (leading to collapse events) and  
886 increase the likelihood of phreatic eruptions (e.g. Day, 1996). The presence of clays can also  
887 reduce the effective pressure required for ductile behavior, resulting in an anomalously shallow  
888 ductile zone that may prevent brittle fracturing and thus volcano-tectonic seismicity prior to some  
889 volcanic eruptions (Mordensky et al., 2019a).

890 A thorough investigation of the type and distribution of alteration is required to highlight  
891 potential source areas for collapse and mass flows events (e.g. debris avalanches and landslides).  
892 The existence of a single vent-hosted hydrothermal system at Mt. Ruapehu suggests that current  
893 (ongoing) hydrothermal alteration may be limited to the active summit crater and conduit (Fig.  
894 11B). However, spectroscopy and aeromagnetic data suggest an abundance of alteration exists in  
895 the upper parts of the south and southeast flanks, either due to lateral fluid migration and/or  
896 older/inactive hydrothermal systems. The mineralogical, hyperspectral and geophysical data all  
897 indicate widespread hydrothermal altered rocks underneath the Summit Plateau, which is likely to  
898 be due to intermediate argillic alteration (Fig. 14B). This alteration is abundant in smectite group  
899 minerals that can precipitate into pores and fractures, thus decreasing rock permeability and  
900 preventing the migration of hydrothermal fluids beneath the Summit Plateau. The reconstructed  
901 mineral suites and hydrothermal alteration map can be combined with ongoing rock mechanical  
902 studies at Mt Ruapehu to provide an improved understanding of the geomechanical properties and  
903 rock mass behavior. This, combined with volume estimates of altered bodies from aeromagnetic  
904 data (Miller et al., 2020b), is vital information for both defining the probability of failures initiating  
905 from these areas and implementing new numerical simulations of mass flows from composite  
906 volcanoes.

907

## 908 **6. Summary and Conclusions**

909

910 The present study integrates alteration mineralogy with hyperspectral imaging and  
911 aeromagnetic data inversion to provide a conceptual model for hydrothermal alteration. These  
912 geophysical and geochemical techniques can also essential to map the 3D distribution of altered  
913 rock masses on composite volcanoes. However, the methods used in this study separately would  
914 not be able to fully describe the hydrothermal alteration. A combined approach is therefore  
915 promoted here to better understand such complex geosystems. This is particularly important for  
916 composite volcanoes with long-lived and nested eruptive centres, which can leave behind relict  
917 hydrothermal systems, potentially invisible on the surface.

918 Hyperspectral imaging is extremely effective at delineating surface hydrothermal alteration  
919 through image classification techniques, allowing quantitative recognition of hydrothermal

920 alteration minerals. Furthermore, airborne imaging system allows very high-resolution imagery to  
921 be acquired, benefitting a detailed spatial mapping of hydrothermal alteration styles due to their  
922 unique combination of mineralogy. However, this technology currently is not capable of assessing  
923 deep-seated hydrothermal alteration and was limited by unconsolidated tephra, snow and ice cover,  
924 and shadow.

925 Aeromagnetic inversion models can complement airborne hyperspectral imaging to quantify  
926 subsurface hydrothermal alteration, by mapping the volume of demagnetized rocks. Hence, the  
927 combination of the airborne remote sensing and geophysical approaches allows the creation of a  
928 detailed, three-dimensional conceptual model for supergene weathering and hydrothermal  
929 alteration processes over the last 200 ky at the Mt Ruapehu volcano.

930 Water saturation can be an important driven for pore pressure fluctuation in volcanic  
931 aquifers. It cannot be detected by aeromagnetic surveys, nor with hyperspectral remote sensing. A  
932 useful add-on can be for future studies to combined those survey techniques above with electrical  
933 and electromagnetic geophysical methods, such as Direct-Current resistivity, induced polarization  
934 and airborne electromagnetics for including groundwater levels water saturation. These methods  
935 need to be included in current monitoring methods to improve our understanding of the trigger  
936 mechanism of slope failures.

937 The detailed surface and subsurface imaging data provide here versatile and high-resolution  
938 baseline information for future studies, which is critical to assess future volcanic activity and  
939 spatial/temporal changes on frequently active volcanoes. The methods used herein can be extended  
940 to other composite volcanoes worldwide. Results from these studies, in combination with  
941 mechanical information on rock-strength, can be applied to identify the volume and configuration  
942 of structurally weak material. Better identification and delineation of flank instability hazards,  
943 obtained through the application of the alteration models, can be used to improve hazard  
944 assessment and mitigation efforts around active volcanoes.

945

## 946 **7. Acknowledgement**

947

948 This study was supported by Natural Hazards Research Platform (“Too big to fail? – A  
949 multidisciplinary approach to predict collapse and debris flow hazards from Mt. Ruapehu”).  
950 C.A.M is also supported by the Ministry of Business, Innovation and Employment-funded GNS  
951 Science Volcanic Hazards Program The authors are grateful for Specim Ltd. for support on image  
952 processing. Field assistance from Abbey Douglas, Marija Voloschina, Soós Ildikó, Ermanno  
953 Brosch, Cecilia Rodriguez-Gomez, Charline Lormand, Boglarka Nemeth, Tyler Barton, Angela  
954 Denes, Emily Koot and Istvan Hajdu is much appreciated. The authors are grateful for the  
955 Department of Conservation, and Iwi around the Tongariro National Park for providing sampling  
956 permits (Authorization Number: 63618-GEO), as well as the Tukino Alpine Sports Club for help  
957 with ground access. Thank you to Michael Rosenberg for sharing XRD data and providing samples  
958 of the ballistic blocks from the 95/96 Ruapehu eruption.

959 The airborne hyperspectral image is publicly available at: [10.5281/zenodo.3905352](https://zenodo.org/record/3905352)

960 The aeromagnetic data is publicly available at  
961 [https://figshare.com/articles/Data and python script/11289149](https://figshare.com/articles/Data_and_python_script/11289149)

962

## 963 **8. References**

964

965 Abdallah, S., Utsugi, M., Aizawa, K., Uyeshima, M., Kanda, W., Koyama, T., and Shiotani, T. (2020). Three-  
966 dimensional electrical resistivity structure of the Kuju volcanic group, Central Kyushu, Japan

- 967 revealed by magnetotelluric survey data. *Journal of Volcanology and Geothermal Research*, 400,  
968 106898. <http://www.sciencedirect.com/science/article/pii/S0377027319305414>
- 969 Ball, J. L., Calder, E. S., Hubbard, B. E., and Bernstein, M. L. (2013). An assessment of hydrothermal  
970 alteration in the Santiaguito lava dome complex, Guatemala: implications for dome collapse  
971 hazards. *Bulletin of Volcanology*, 75(1), 676. <https://doi.org/10.1007/s00445-012-0676-z>
- 972 Ball, J. L., Taron, J., Reid, M. E., Hurwitz, S., Finn, C., and Bedrosian, P. (2018). Combining Multiphase  
973 Groundwater Flow and Slope Stability Models to Assess Stratovolcano Flank Collapse in the  
974 Cascade Range. *Journal of Geophysical Research: Solid Earth*, 123(4), 2787-2805.  
975 <https://agupubs.onlinelibrary.wiley.com/doi/abs/10.1002/2017JB015156>
- 976 Beauchamps, G., Ledésert, B., Hébert, R., Navelot, V., and Favier, A. (2019). The characterisation of an  
977 exhumed high-temperature paleo-geothermal system on Terre-de-Haut Island (the Les Saintes  
978 archipelago, Guadeloupe) in terms of clay minerals and petrophysics. *Geothermal Energy*, 7(1),  
979 6. journal article. <https://doi.org/10.1186/s40517-019-0122-y>
- 980 Belgiu, M., and Drăguț, L. (2016). Random forest in remote sensing: A review of applications and future  
981 directions. *ISPRS Journal of Photogrammetry and Remote Sensing*, 114, 24-31.  
982 <http://www.sciencedirect.com/science/article/pii/S0924271616000265>
- 983 Berlo, K., van Hinsberg, V., Suparjan, Purwanto, B. H., and Gunawan, H. (2020). Using the composition of  
984 fluid seepage from the magmatic-hydrothermal system of Kawah Ijen volcano, Indonesia, as a  
985 monitoring tool. *Journal of Volcanology and Geothermal Research*, 399, 106899.  
986 <http://www.sciencedirect.com/science/article/pii/S0377027319306353>
- 987 Bishop, J., L., and Murad, E. (2005). The visible and infrared spectral properties of jarosite and alunite. In  
988 *American Mineralogist* (Vol. 90, pp. 1100).
- 989 Bladh, K. W. (1982). The formation of goethite, jarosite, and alunite during the weathering of sulfide-  
990 bearing felsic rocks. *Economic Geology*, 77(1), 176-184.  
991 <https://doi.org/10.2113/gsecongeo.77.1.176>
- 992 Bouzari, F., Hart, C. J. R., Bissig, T., and Barker, S. (2016). Hydrothermal Alteration Revealed by Apatite  
993 Luminescence and Chemistry: A Potential Indicator Mineral for Exploring Covered Porphyry  
994 Copper Deposits. *Economic Geology*, 111(6), 1397-1410.  
995 <https://doi.org/10.2113/econgeo.111.6.1397>
- 996 Bowles-Martinez, E., and Schultz, A. (2020). Composition of Magma and Characteristics of the  
997 Hydrothermal System of Newberry Volcano, Oregon, From Magnetotellurics. *Geochemistry,*  
998 *Geophysics, Geosystems*, 21(3), e2019GC008831.  
999 <https://agupubs.onlinelibrary.wiley.com/doi/abs/10.1029/2019GC008831>
- 1000 Boyce, A. J., Fulignati, P., Sbrana, A., and Fallick, A. E. (2007). Fluids in early stage hydrothermal  
1001 alteration of high-sulfidation epithermal systems: A view from the Vulcano active hydrothermal  
1002 system (Aeolian Island, Italy). *Journal of Volcanology and Geothermal Research*, 166(2), 76-90.  
1003 <http://www.sciencedirect.com/science/article/pii/S0377027307002181>
- 1004 Brady, K. S., Bigham, J. M., Jaynes, W. F., and Logan, T. J. (1986). Influence of Sulfate on Fe-Oxide  
1005 Formation: Comparisons with a Stream Receiving Acid Mine Drainage. *Clays and Clay Minerals*,  
1006 34(3), 266-274. <https://doi.org/10.1346/CCMN.1986.0340306>
- 1007 Breiman, L. (2001). Random Forests. *Machine Learning*, 45(1), 5-32. journal article.  
1008 <http://dx.doi.org/10.1023/A:1010933404324>
- 1009 Buddington, A. F., and Lindsley, D. H. (1964). Iron-Titanium Oxide Minerals and Synthetic Equivalents.  
1010 *Journal of Petrology*, 5(2), 310-357. <https://doi.org/10.1093/petrology/5.2.310>
- 1011 Capra, L. (2006). Abrupt climatic changes as triggering mechanisms of massive volcanic collapses. *Journal*  
1012 *of Volcanology and Geothermal Research*, 155(3), 329-333.  
1013 <http://www.sciencedirect.com/science/article/pii/S0377027306001855>

- 1014 Carrino, T. A., Crósta, A. P., Toledo, C. L. B., and Silva, A. M. (2018). Hyperspectral remote sensing  
1015 applied to mineral exploration in southern Peru: A multiple data integration approach in the  
1016 Chapi Chiara gold prospect. *International Journal of Applied Earth Observation and*  
1017 *Geoinformation*, 64, 287-300.  
1018 <http://www.sciencedirect.com/science/article/pii/S0303243417301071>
- 1019 Cassidy, M., Manga, M., Cashman, K., and Bachmann, O. (2018). Controls on explosive-effusive volcanic  
1020 eruption styles. *Nature Communications*, 9(1), 2839. [https://doi.org/10.1038/s41467-018-](https://doi.org/10.1038/s41467-018-05293-3)  
1021 [05293-3](https://doi.org/10.1038/s41467-018-05293-3)
- 1022 Christenson, B. W. (2000). Geochemistry of fluids associated with the 1995–1996 eruption of Mt.  
1023 Ruapehu, New Zealand: signatures and processes in the magmatic-hydrothermal system. *Journal*  
1024 *of Volcanology and Geothermal Research*, 97(1), 1-30.  
1025 <http://www.sciencedirect.com/science/article/pii/S0377027399001675>
- 1026 Christenson, B. W., Reyes, A. G., Young, R., Moebis, A., Sherburn, S., Cole-Baker, J., and Britten, K.  
1027 (2010). Cyclic processes and factors leading to phreatic eruption events: Insights from the 25  
1028 September 2007 eruption through Ruapehu Crater Lake, New Zealand. *Journal of Volcanology*  
1029 *and Geothermal Research*, 191(1), 15-32.  
1030 <http://www.sciencedirect.com/science/article/pii/S0377027310000223>
- 1031 Christenson, B. W., and Wood, C. P. (1993). Evolution of a vent-hosted hydrothermal system beneath  
1032 Ruapehu Crater Lake, New Zealand. *Bulletin of Volcanology*, 55(8), 547-565. journal article.  
1033 <https://doi.org/10.1007/BF00301808>
- 1034 Clark, R. N., Gallagher, A. J., and Swayze, G. A. (1990). Material absorption band depth mapping of  
1035 imaging spectrometer data using the complete band shape least-squares algorithm  
1036 simultaneously fit to multiple spectral features from multiple materials. *Proceedings of the Third*  
1037 *Airborne Visible/Infrared Imaging Spectrometer (AVIRIS) Workshop, JPL Publication 90-54*, 176-  
1038 186.
- 1039 Clark, R. N., and Roush, T. L. (1984). Reflectance spectroscopy: Quantitative analysis techniques for  
1040 remote sensing applications. *Journal of Geophysical Research: Solid Earth*, 89(B7), 6329-6340.  
1041 <https://agupubs.onlinelibrary.wiley.com/doi/abs/10.1029/JB089iB07p06329>
- 1042 Clark, R. N., Swayze, G. A., Livo, K. E., Kokaly, R. F., Sutley, S. J., Dalton, J. B., et al. (2003). Imaging  
1043 spectroscopy: Earth and planetary remote sensing with the USGS Tetracorder and expert  
1044 systems. *Journal of Geophysical Research E: Planets*, 108(12), 1-44.  
1045 <http://pubs.er.usgs.gov/publication/70025059>
- 1046 Cockett, R., Kang, S., Heagy, L. J., Pidlisecky, A., and Oldenburg, D. W. (2015). SimPEG: An open source  
1047 framework for simulation and gradient based parameter estimation in geophysical applications.  
1048 *Computers & Geosciences*, 85, 142-154.  
1049 <http://www.sciencedirect.com/science/article/pii/S009830041530056X>
- 1050 Collard, N., Peiffer, L., and Taran, Y. (2020). Heat and fluid flow dynamics of a stratovolcano: The Tacaná  
1051 Volcanic Complex, Mexico-Guatemala. *Journal of Volcanology and Geothermal Research*, 400,  
1052 106916. <http://www.sciencedirect.com/science/article/pii/S0377027320300652>
- 1053 Conway, C. E., Gamble, J. A., Wilson, C. J. N., Leonard, G. S., Townsend, D. B., and Calvert, A. T. (2018).  
1054 New petrological, geochemical, and geochronological perspectives on andesite-dacite magma  
1055 genesis at Ruapehu volcano, New Zealand. *American Mineralogist*, 103(4), 565-581.  
1056 <https://doi.org/10.2138/am-2018-6199>
- 1057 Conway, C. E., Leonard, G. S., Townsend, D. B., Calvert, A. T., Wilson, C. J. N., Gamble, J. A., and Eaves, S.  
1058 R. (2016). A high-resolution <sup>40</sup>Ar/<sup>39</sup>Ar lava chronology and edifice construction history for  
1059 Ruapehu volcano, New Zealand. *Journal of Volcanology and Geothermal Research*, 327, 152-179.  
1060 <http://www.sciencedirect.com/science/article/pii/S0377027316302062>

- 1061 Cronin, S. J., Neall, V. E., Lecointre, J. A., and Palmer, A. S. (1997). Changes in Whangaehu river lahar  
1062 characteristics during the 1995 eruption sequence, Ruapehu volcano, New Zealand. *Journal of*  
1063 *Volcanology and Geothermal Research*, 76(1), 47-61.  
1064 <http://www.sciencedirect.com/science/article/pii/S0377027396000649>
- 1065 Crosta, A. P., Sabine, C., and Taranik, J. V. (1998). Hydrothermal Alteration Mapping at Bodie, California,  
1066 using AVIRIS Hyperspectral Data. *Remote Sensing of Environment*, 65(3), 309–319.
- 1067 Crowley, J. K., Hubbard, B. E., and Mars, J. C. (2003). Analysis of potential debris flow source areas on  
1068 Mount Shasta, California, by using airborne and satellite remote sensing data. *Remote Sensing of*  
1069 *Environment*, 87(2–3), 345-358.  
1070 [//www.sciencedirect.com/science/article/pii/S0034425703001925](http://www.sciencedirect.com/science/article/pii/S0034425703001925)
- 1071 Day, S. J. (1996). Hydrothermal pore fluid pressure and the stability of porous, permeable volcanoes.  
1072 *Geological Society, London, Special Publications*, 110(1), 77-93.  
1073 <https://sp.lyellcollection.org/content/specpubgsl/110/1/77.full.pdf>
- 1074 del Potro, R., and Hürlimann, M. (2009). The decrease in the shear strength of volcanic materials with  
1075 argillic hydrothermal alteration, insights from the summit region of Teide stratovolcano,  
1076 Tenerife. *Engineering Geology*, 104(1), 135-143.  
1077 <http://www.sciencedirect.com/science/article/pii/S0013795208002457>
- 1078 Dill, H. G. (2001). The geology of aluminium phosphates and sulphates of the alunite group minerals: a  
1079 review. *Earth-Science Reviews*, 53(1), 35-93.  
1080 <http://www.sciencedirect.com/science/article/pii/S0012825200000350>
- 1081 Dill, H. G. (2016). Kaolin: Soil, rock and ore: From the mineral to the magmatic, sedimentary and  
1082 metamorphic environments. *Earth-Science Reviews*, 161, 16-129.  
1083 <http://www.sciencedirect.com/science/article/pii/S0012825216301568>
- 1084 Donoghue, S. L., and Neall, V. E. (1996). Tephrostratigraphic studies at Tongariro Volcanic Centre, New  
1085 Zealand: An overview. *Quaternary International*, 34–36(0), 13-20.  
1086 <http://www.sciencedirect.com/science/article/pii/1040618295000658>
- 1087 Donoghue, S. L., and Neall, V. E. (2001). Late Quaternary constructional history of the southeastern  
1088 Ruapehu ring plain, New Zealand. *New Zealand Journal of Geology and Geophysics*, 44(3), 439-  
1089 466. <https://doi.org/10.1080/00288306.2001.9514949>
- 1090 Ece, Ö. I., Çoban, F., Güngör, N., and Suner, F. (1999). Clay Mineralogy and Occurrence of Ferrian  
1091 Smectites Between Serpentinite Saprolites and Basalts in Biga Peninsula, Northwest Turkey.  
1092 *Clays and Clay Minerals*, 47(3), 241-251. journal article.  
1093 <https://doi.org/10.1346/CCMN.1999.0470301>
- 1094 Farquharson, J. I., Baud, P., and Heap, M. J. (2017). Inelastic compaction and permeability evolution in  
1095 volcanic rock. *Solid Earth*, 8(2), 561-581. <https://se.copernicus.org/articles/8/561/2017/>
- 1096 Farquharson, J. I., Wild, B., Kushnir, A. R. L., Heap, M. J., Baud, P., and Kennedy, B. (2019). Acid-Induced  
1097 Dissolution of Andesite: Evolution of Permeability and Strength. *Journal of Geophysical*  
1098 *Research: Solid Earth*, 124(1), 257-273.  
1099 <https://agupubs.onlinelibrary.wiley.com/doi/abs/10.1029/2018JB016130>
- 1100 Fernández-Caliani, J. C., Crespo, E., Rodas, M., Barrenechea, J. F., and Luque, F. J. (2004). Formation of  
1101 Nontronite from Oxidative Dissolution of Pyrite Disseminated in Precambrian Felsic  
1102 Metavolcanics of the Southern Iberian Massif (Spain). *Clays and Clay Minerals*, 52(1), 106-114.  
1103 <https://doi.org/10.1346/CCMN.2004.0520110>
- 1104 Fernández-Caliani, J. C., Crespo, E., Rodas, M., Barrenechea, J. F., and Luque, F. J. (2004). Formation of  
1105 nontronite from oxidative dissolution of pyrite disseminated in precambrian felsic metavolcanics  
1106 of the southern Iberian Massif (Spain). *Clays and Clay Minerals*, 52(1), 106-114.  
1107 <https://doi.org/10.1346/CCMN.2004.0520110>

- 1108 Finn, C. A., Deszcz-Pan, M., Ball, J. L., Bloss, B. J., and Minsley, B. J. (2018). Three-dimensional  
 1109 geophysical mapping of shallow water saturated altered rocks at Mount Baker, Washington:  
 1110 Implications for slope stability. *Journal of Volcanology and Geothermal Research*, 357, 261-275.  
 1111 <http://www.sciencedirect.com/science/article/pii/S0377027317307199>
- 1112 Finn, C. A., Sisson, T. W., and Deszcz-Pan, M. (2001). Aerogeophysical measurements of collapse-prone  
 1113 hydrothermally altered zones at Mount Rainier volcano. *Nature*, 409(6820), 600-603.  
 1114 [10.1038/35054533](http://dx.doi.org/10.1038/35054533). <http://dx.doi.org/10.1038/35054533>
- 1115 Fournier, D., Heagy, L. J., and Oldenburg, D. W. (2020). Sparse magnetic vector inversion in spherical  
 1116 coordinates. *Geophysics*, 85(3), J33-J49. [https://library.seg.org/doi/abs/10.1190/geo2019-](https://library.seg.org/doi/abs/10.1190/geo2019-0244.1)  
 1117 [0244.1](https://library.seg.org/doi/abs/10.1190/geo2019-0244.1)
- 1118 Galvão, L. S., Almeida-Filho, R., and Vitorello, Í. (2005). Spectral discrimination of hydrothermally altered  
 1119 materials using ASTER short-wave infrared bands: Evaluation in a tropical savannah  
 1120 environment. *International Journal of Applied Earth Observation and Geoinformation*, 7(2), 107-  
 1121 114. <http://www.sciencedirect.com/science/article/pii/S0303243405000310>
- 1122 Gamble, J. A., Price, R. C., Smith, I. E. M., McIntosh, W. C., and Dunbar, N. W. (2003). 40Ar/39Ar  
 1123 geochronology of magmatic activity, magma flux and hazards at Ruapehu volcano, Taupo  
 1124 Volcanic Zone, New Zealand. *Journal of Volcanology and Geothermal Research*, 120(3-4), 271-  
 1125 287. Article. [https://www.scopus.com/inward/record.uri?eid=2-s2.0-](https://www.scopus.com/inward/record.uri?eid=2-s2.0-0037303551&partnerID=40&md5=8c7c5f379bf6d40a9c3ac02f1552839e)  
 1126 [0037303551&partnerID=40&md5=8c7c5f379bf6d40a9c3ac02f1552839e](https://www.scopus.com/inward/record.uri?eid=2-s2.0-0037303551&partnerID=40&md5=8c7c5f379bf6d40a9c3ac02f1552839e)
- 1127 Gamble, J. A., Wood, C. P., Price, R. C., Smith, I. E. M., Stewart, R. B., and Waight, T. (1999). A fifty year  
 1128 perspective of magmatic evolution on Ruapehu Volcano, New Zealand: verification of open  
 1129 system behaviour in an arc volcano. *Earth and Planetary Science Letters*, 170(3), 301-314.  
 1130 <http://www.sciencedirect.com/science/article/pii/S0012821X99001065>
- 1131 Ganino, C., Libourel, G., and Bernard, A. (2019). Fumarolic incrustations at Kudryavy volcano  
 1132 (Kamchatka) as a guideline for high-temperature (>850 °C) extinct hydrothermal systems.  
 1133 *Journal of Volcanology and Geothermal Research*, 376, 75-85.  
 1134 <http://www.sciencedirect.com/science/article/pii/S0377027319300058>
- 1135 Graham, I. J., and Hackett, W. R. (1987). Petrology of Calc-alkaline Lavas from Ruapehu Volcano and  
 1136 Related Vents, Taupo Volcanic Zone, New Zealand. *Journal of Petrology*, 28(3), 531-567.  
 1137 <https://doi.org/10.1093/petrology/28.3.531>
- 1138 Gresse, M., Vandemeulebrouck, J., Byrdina, S., Chiodini, G., Roux, P., Rinaldi, A. P., et al. (2018).  
 1139 Anatomy of a fumarolic system inferred from a multiphysics approach. *Scientific Reports*, 8(1),  
 1140 7580. <https://doi.org/10.1038/s41598-018-25448-y>
- 1141 Hackett, W. R., and Houghton, B. F. (1989). A facies model for a quaternary andesitic composite volcano:  
 1142 Ruapehu, New Zealand. *Bulletin of Volcanology*, 51(1), 51-68. journal article.  
 1143 <http://dx.doi.org/10.1007/BF01086761>
- 1144 Heap, M. J., Gravley, D. M., Kennedy, B. M., Gilg, H. A., Bertolett, E., and Barker, S. L. L. (2020).  
 1145 Quantifying the role of hydrothermal alteration in creating geothermal and epithermal mineral  
 1146 resources: The Ohakuri ignimbrite (Taupō Volcanic Zone, New Zealand). *Journal of Volcanology*  
 1147 *and Geothermal Research*, 390, 106703.  
 1148 <http://www.sciencedirect.com/science/article/pii/S0377027319304688>
- 1149 Heap, M. J., Kennedy, B. M., Pernin, N., Jacquemard, L., Baud, P., Farquharson, J. I., et al. (2015).  
 1150 Mechanical behaviour and failure modes in the Whakaari (White Island volcano) hydrothermal  
 1151 system, New Zealand. *Journal of Volcanology and Geothermal Research*, 295, 26-42. Article.  
 1152 [https://www.scopus.com/inward/record.uri?eid=2-s2.0-](https://www.scopus.com/inward/record.uri?eid=2-s2.0-84924873678&doi=10.1016%2Fj.jvolgeores.2015.02.012&partnerID=40&md5=703e2dab063ab2643eee69f8ab7d0d9d)  
 1153 [84924873678&doi=10.1016%2Fj.jvolgeores.2015.02.012&partnerID=40&md5=703e2dab063ab2](https://www.scopus.com/inward/record.uri?eid=2-s2.0-84924873678&doi=10.1016%2Fj.jvolgeores.2015.02.012&partnerID=40&md5=703e2dab063ab2643eee69f8ab7d0d9d)  
 1154 [643eee69f8ab7d0d9d](https://www.scopus.com/inward/record.uri?eid=2-s2.0-84924873678&doi=10.1016%2Fj.jvolgeores.2015.02.012&partnerID=40&md5=703e2dab063ab2643eee69f8ab7d0d9d)

- 1155 Heap, M. J., Troll, V. R., Kushnir, A. R. L., Gilg, H. A., Collinson, A. S. D., Deegan, F. M., et al. (2019).  
1156 Hydrothermal alteration of andesitic lava domes can lead to explosive volcanic behaviour.  
1157 *Nature Communications*, 10(1), 5063. <https://doi.org/10.1038/s41467-019-13102-8>
- 1158 Hellman, M. J., and Ramsey, M. S. (2004). Analysis of hot springs and associated deposits in Yellowstone  
1159 National Park using ASTER and AVIRIS remote sensing. *Journal of Volcanology and Geothermal*  
1160 *Research*, 135(1–2), 195–219.  
1161 <http://www.sciencedirect.com/science/article/pii/S037702730400037X>
- 1162 Hunt, G. R., and Ashley, R. P. (1979). Spectra of altered rocks in the visible and near infrared. *Economic*  
1163 *Geology*, 74(7), 1613–1629. <https://doi.org/10.2113/gsecongeo.74.7.1613>
- 1164 Hynek, B. M., McCollom, T. M., Marcucci, E. C., Brugman, K., and Rogers, K. L. (2013). Assessment of  
1165 environmental controls on acid-sulfate alteration at active volcanoes in Nicaragua: Applications  
1166 to relic hydrothermal systems on Mars. *Journal of Geophysical Research: Planets*, 118(10), 2083–  
1167 2104. <https://agupubs.onlinelibrary.wiley.com/doi/abs/10.1002/jgre.20140>
- 1168 Imura, T., Minami, Y., Ohba, T., Matsumoto, A., Arribas, A., and Nakagawa, M. (2019). Hydrothermal  
1169 Aluminum-Phosphate-Sulfates in Ash from the 2014 Hydrothermal Eruption at Ontake Volcano,  
1170 Central Honshu, Japan. *Minerals*, 9(8), 462. <https://www.mdpi.com/2075-163X/9/8/462>
- 1171 Ingham, M. R., Bibby, H. M., Heise, W., Jones, K. A., Cairns, P., Dravitzki, S., et al. (2009). A  
1172 magnetotelluric study of Mount Ruapehu volcano, New Zealand. *Geophysical Journal*  
1173 *International*, 179(2), 887–904. [https://onlinelibrary.wiley.com/doi/abs/10.1111/j.1365-](https://onlinelibrary.wiley.com/doi/abs/10.1111/j.1365-246X.2009.04317.x)  
1174 [246X.2009.04317.x](https://onlinelibrary.wiley.com/doi/abs/10.1111/j.1365-246X.2009.04317.x)
- 1175 Inostroza, M., Aguilera, F., Menzies, A., Layana, S., González, C., Ureta, G., et al. (2020). Deposition of  
1176 metals and metalloids in the fumarolic fields of Guallatiri and Lastarria volcanoes, northern  
1177 Chile. *Journal of Volcanology and Geothermal Research*, 393, 106803.  
1178 <http://www.sciencedirect.com/science/article/pii/S0377027319304536>
- 1179 James, M. R., and Robson, S. (2012). Straightforward reconstruction of 3D surfaces and topography with  
1180 a camera: Accuracy and geoscience application. *Journal of Geophysical Research: Earth Surface*,  
1181 117(F3), 1–17. <http://dx.doi.org/10.1029/2011JF002289>
- 1182 John, D. A., Lee, R. G., Breit, G. N., Dilles, J. H., Calvert, A. T., Muffler, L. J. P., and Clynne, M. A. (2019).  
1183 Pleistocene hydrothermal activity on Brokeoff volcano and in the Maidu volcanic center, Lassen  
1184 Peak area, northeast California: Evolution of magmatic-hydrothermal systems on  
1185 stratovolcanoes. *Geosphere*, 15(3), 946–982. <https://doi.org/10.1130/GES02049.1>
- 1186 John, D. A., Sisson, T. W., Breit, G. N., Rye, R. O., and Vallance, J. W. (2008). Characteristics, extent and  
1187 origin of hydrothermal alteration at Mount Rainier Volcano, Cascades Arc, USA: Implications for  
1188 debris-flow hazards and mineral deposits. *Journal of Volcanology and Geothermal Research*,  
1189 175(3), 289–314. <http://www.sciencedirect.com/science/article/pii/S0377027308001200>
- 1190 Johnston, D. M., Houghton, B. F., Neall, V. E., Ronan, K. R., and Paton, D. (2000). Impacts of the 1945 and  
1191 1995–1996 Ruapehu eruptions, New Zealand: An example of increasing societal vulnerability.  
1192 *Geological Society of America Bulletin*, 112(5), 720–726.  
1193 <http://gsabulletin.gsapubs.org/content/112/5/720.abstract>
- 1194 Jones, K. A., Ingham, M. R., and Bibby, H. M. (2008). The hydrothermal vent system of Mount Ruapehu,  
1195 New Zealand — a high frequency MT survey of the summit plateau. *Journal of Volcanology and*  
1196 *Geothermal Research*, 176(4), 591–600.  
1197 <http://www.sciencedirect.com/science/article/pii/S0377027308002643>
- 1198 Kereszturi, G., Schaefer, L. N., Schleiffarth, W. K., Procter, J., Pullanagari, R. R., Mead, S., and Kennedy, B.  
1199 (2018). Integrating airborne hyperspectral imagery and LiDAR for volcano mapping and  
1200 monitoring through image classification. *International Journal of Applied Earth Observation and*  
1201 *Geoinformation*, 73, 323–339.  
1202 <http://www.sciencedirect.com/science/article/pii/S0303243418305300>

- 1203 Kilgour, G., Blundy, J., Cashman, K., and Mader, H. M. (2013). Small volume andesite magmas and melt–  
 1204 melt interactions at Ruapehu, New Zealand: evidence from melt inclusions. *Contributions to*  
 1205 *Mineralogy and Petrology*, 166(2), 371-392. <https://doi.org/10.1007/s00410-013-0880-7>
- 1206 Kokaly, R. F., Clark, R. N., Swayze, G. A., Livo, K. E., Hoefen, T. M., Pearson, N. C., et al. (2017). *USGS*  
 1207 *Spectral Library Version 7* (1035). Retrieved from Reston, VA:  
 1208 <http://pubs.er.usgs.gov/publication/ds1035>
- 1209 Kruse, F. A., Baugh, W. M., and Perry, S. L. (2015). Validation of DigitalGlobe WorldView-3 Earth imaging  
 1210 satellite shortwave infrared bands for mineral mapping. *Journal of Applied Remote Sensing*, 9(1),  
 1211 1-17.
- 1212 Le Gonidec, Y., Rosas-Carbajal, M., Bremond d’Ars, J. d., Carlus, B., Ianigro, J. C., Kergosien, B., et al.  
 1213 (2019). Abrupt changes of hydrothermal activity in a lava dome detected by combined seismic  
 1214 and muon monitoring. *Scientific Reports*, 9(1), 3079. [https://doi.org/10.1038/s41598-019-](https://doi.org/10.1038/s41598-019-39606-3)  
 1215 [39606-3](https://doi.org/10.1038/s41598-019-39606-3)
- 1216 Liu, C., Frazier, P., and Kumar, L. (2007). Comparative assessment of the measures of thematic  
 1217 classification accuracy. *Remote Sensing of Environment*, 107(4), 606-616.  
 1218 <http://www.sciencedirect.com/science/article/pii/S0034425706004068>
- 1219 López, D. L., and Williams, S. N. (1993). Catastrophic Volcanic Collapse: Relation to Hydrothermal  
 1220 Processes. *Science*, 260(5115), 1794-1796.  
 1221 <https://science.sciencemag.org/content/sci/260/5115/1794.full.pdf>
- 1222 Matsunaga, Y., Kanda, W., Takakura, S., Koyama, T., Saito, Z., Seki, K., et al. (2020). Magmatic  
 1223 hydrothermal system inferred from the resistivity structure of Kusatsu-Shirane Volcano. *Journal*  
 1224 *of Volcanology and Geothermal Research*, 390, 106742.  
 1225 <http://www.sciencedirect.com/science/article/pii/S0377027319303312>
- 1226 Mavrogenes, J., and Blundy, J. (2017). Crustal sequestration of magmatic sulfur dioxide. *Geology*, 45(3),  
 1227 211-214. <https://doi.org/10.1130/G38555.1>
- 1228 Mayer, K., Scheu, B., Yilmaz, T. I., Montanaro, C., Albert Gilg, H., Rott, S., et al. (2017). Phreatic activity  
 1229 and hydrothermal alteration in the Valley of Desolation, Dominica, Lesser Antilles. *Bulletin of*  
 1230 *Volcanology*, 79(12), 82. <https://doi.org/10.1007/s00445-017-1166-0>
- 1231 Mia, B., and Fujimitsu, Y. (2012). Mapping hydrothermal altered mineral deposits using Landsat 7 ETM+  
 1232 image in and around Kuju volcano, Kyushu, Japan. *Journal of Earth System Science*, 121(4), 1049-  
 1233 1057. <https://doi.org/10.1007/s12040-012-0211-9>
- 1234 Miller, C. A., Christenson, B. W., Byrdina, S., Vandemeulebrouck, J., Brakenrig, T., Britten, K., et al.  
 1235 (2020a). Snapshot of a magmatic/hydrothermal system from electrical resistivity tomography  
 1236 and fumarolic composition, Whakaari/White Island, New Zealand. *Journal of Volcanology and*  
 1237 *Geothermal Research*, 400, 106909.  
 1238 <http://www.sciencedirect.com/science/article/pii/S0377027320301529>
- 1239 Miller, C. A., Kang, S. G., Fournier, D., and Hill, G. (2018). Distribution of Vapor and Condensate in a  
 1240 Hydrothermal System: Insights From Self-Potential Inversion at Mount Tongariro, New Zealand.  
 1241 *Geophysical Research Letters*, 45(16), 8190-8198.  
 1242 <https://agupubs.onlinelibrary.wiley.com/doi/abs/10.1029/2018GL078780>
- 1243 Miller, C. A., Schaefer, L. N., Kereszturi, G., and Fournier, D. (2020b). Three-Dimensional Mapping of Mt.  
 1244 Ruapehu Volcano, New Zealand, From Aeromagnetic Data Inversion and Hyperspectral Imaging.  
 1245 *Journal of Geophysical Research: Solid Earth*, 125(2), e2019JB018247.  
 1246 <https://doi.org/10.1029/2019JB018247>
- 1247 Miller, C. A., and Williams-Jones, G. (2016). Internal structure and volcanic hazard potential of Mt  
 1248 Tongariro, New Zealand, from 3D gravity and magnetic models. *Journal of Volcanology and*  
 1249 *Geothermal Research*, 319, 12-28.  
 1250 [//www.sciencedirect.com/science/article/pii/S0377027316300245](http://www.sciencedirect.com/science/article/pii/S0377027316300245)

- 1251 Mitchell, A. C., Lafrenière, M. J., Skidmore, M. L., and Boyd, E. S. (2013). Influence of bedrock mineral  
1252 composition on microbial diversity in a subglacial environment. *Geology*, 41(8), 855-858.  
1253 <https://doi.org/10.1130/G34194.1>
- 1254 Moore, P. R., and Brock, J. L. (1981). A physical and chemical survey of Ketetahi Hot Springs, Mt  
1255 Tongariro, New Zealand. *New Zealand Journal of Science*, 24(2), 161-177.
- 1256 Mordensky, S. P., Heap, M. J., Kennedy, B. M., Gilg, H. A., Villeneuve, M. C., Farquharson, J. I., and  
1257 Gravelly, D. M. (2019a). Influence of alteration on the mechanical behaviour and failure mode of  
1258 andesite: implications for shallow seismicity and volcano monitoring. *Bulletin of Volcanology*,  
1259 81(8), 44. journal article. <https://doi.org/10.1007/s00445-019-1306-9>
- 1260 Mordensky, S. P., Kennedy, B. M., Villeneuve, M. C., Lavallée, Y., Reichow, M. K., Wallace, P. A., et al.  
1261 (2019b). Increasing the Permeability of Hydrothermally Altered Andesite by Transitory Heating.  
1262 *Geochemistry, Geophysics, Geosystems*, 20(11), 5251-5269.  
1263 <https://agupubs.onlinelibrary.wiley.com/doi/abs/10.1029/2019GC008409>
- 1264 Murowchick, J. B., and Barnes, H. L. (1987). Effects of temperature and degree of supersaturation on  
1265 pyrite morphology. *American Mineralogist*, 72(11-12), 1241-1250.
- 1266 Murphy, R. J., Taylor, Z., Schneider, S., and Nieto, J. (2015). Mapping clay minerals in an open-pit mine  
1267 using hyperspectral and LiDAR data. *European Journal of Remote Sensing*, 48(1), 511-526.  
1268 <https://doi.org/10.5721/EuJRS20154829>
- 1269 Nakagawa, M., Wada, K., Thordarson, T., Wood, C. P., and Gamble, J. A. (1999). Petrologic investigations  
1270 of the 1995 and 1996 eruptions of Ruapehu volcano, New Zealand: formation of discrete and  
1271 small magma pockets and their intermittent discharge. *Bulletin of Volcanology*, 61(1), 15-31.  
1272 <https://doi.org/10.1007/s004450050259>
- 1273 Neal, L. C., Wilkinson, J. J., Mason, P. J., and Chang, Z. (2018). Spectral characteristics of propylitic  
1274 alteration minerals as a vectoring tool for porphyry copper deposits. *Journal of Geochemical*  
1275 *Exploration*, 184, 179-198.  
1276 <http://www.sciencedirect.com/science/article/pii/S0375674216303958>
- 1277 Noack, Y., Colin, F., Nahon, D., Delvigne, J., and Michaux, L. (1993). Secondary-mineral formation during  
1278 natural weathering of pyroxene; review and thermodynamic approach. *American Journal of*  
1279 *Science*, 293(2), 111-134. <http://www.ajsonline.org/content/293/2/111.short>
- 1280 Nordstrom, D. (1982). Aqueous pyrite oxidation and the consequent formation of secondary minerals. In  
1281 (Vol. 10, pp. 37-56).
- 1282 Norini, G., Bustos, E., Arnosio, M., Baez, W., Zuluaga, M. C., and Roverato, M. (2020). Unusual volcanic  
1283 instability and sector collapse configuration at Chimpa volcano, central Andes. *Journal of*  
1284 *Volcanology and Geothermal Research*, 393, 106807.  
1285 <http://www.sciencedirect.com/science/article/pii/S0377027319306377>
- 1286 Nuñez-Hernández, S., Pinti, D. L., López-Hernández, A., Shouakar-Stash, O., Martínez-Cinco, M. A.,  
1287 Abuharara, A., et al. (2020). Phase segregation, boiling, and reinjection at the Los Azufres  
1288 Geothermal Field, Mexico, monitored by water stable isotopes, chloride, and enthalpy. *Journal*  
1289 *of Volcanology and Geothermal Research*, 390, 106751.  
1290 <http://www.sciencedirect.com/science/article/pii/S0377027319300149>
- 1291 Okujeni, A., van der Linden, S., Tits, L., Somers, B., and Hostert, P. (2013). Support vector regression and  
1292 synthetically mixed training data for quantifying urban land cover. *Remote Sensing of*  
1293 *Environment*, 137, 184-197.  
1294 <http://www.sciencedirect.com/science/article/pii/S0034425713002009>
- 1295 Okumura, S., and Sasaki, O. (2014). Permeability reduction of fractured rhyolite in volcanic conduits and  
1296 its control on eruption cyclicity. *Geology*, 42(10), 843-846. <https://doi.org/10.1130/G35855.1>
- 1297 Pal, M. (2005). Random forest classifier for remote sensing classification. *International Journal of*  
1298 *Remote Sensing*, 26(1), 217-222. <http://dx.doi.org/10.1080/01431160412331269698>

- 1299 Palmer, B. A., and Neall, V. E. (1989). The Murimotu Formation—9500 year old deposits of a debris  
 1300 avalanche and associated lahars, Mount Ruapehu, North Island, New Zealand. *New Zealand*  
 1301 *Journal of Geology and Geophysics*, 32(4), 477-486.  
 1302 <https://doi.org/10.1080/00288306.1989.10427555>
- 1303 Pardo, N., Cronin, S., Palmer, A., Procter, J., and Smith, I. (2012). Andesitic Plinian eruptions at Mt.  
 1304 Ruapehu: quantifying the uppermost limits of eruptive parameters. *Bulletin of Volcanology*,  
 1305 74(5), 1161-1185. <http://dx.doi.org/10.1007/s00445-012-0588-y>
- 1306 Pardo, N., Cronin, S. J., Németh, K., Brenna, M., Schipper, C. I., Breard, E., et al. (2014). Perils in  
 1307 distinguishing phreatic from phreatomagmatic ash; insights into the eruption mechanisms of the  
 1308 6 August 2012 Mt. Tongariro eruption, New Zealand. *Journal of Volcanology and Geothermal*  
 1309 *Research*, 286, 397-414. <http://www.sciencedirect.com/science/article/pii/S037702731400136X>
- 1310 Piccoli, P. M., and Candela, P. A. (2002). Apatite in Igneous Systems. *Reviews in Mineralogy and*  
 1311 *Geochemistry*, 48(1), 255-292. <https://doi.org/10.2138/rmg.2002.48.6>
- 1312 Piochi, M., Mormone, A., and Balassone, G. (2019). Hydrothermal alteration environments and recent  
 1313 dynamics of the Ischia volcanic island (southern Italy): Insights from repeated field,  
 1314 mineralogical and geochemical surveys before and after the 2017 Casamicciola earthquake.  
 1315 *Journal of Volcanology and Geothermal Research*, 376, 104-124.  
 1316 <http://www.sciencedirect.com/science/article/pii/S0377027318303263>
- 1317 Piochi, M., Mormone, A., Balassone, G., Strauss, H., Troise, C., and De Natale, G. (2015). Native sulfur,  
 1318 sulfates and sulfides from the active Campi Flegrei volcano (southern Italy): Genetic  
 1319 environments and degassing dynamics revealed by mineralogy and isotope geochemistry.  
 1320 *Journal of Volcanology and Geothermal Research*, 304, 180-193.  
 1321 <http://www.sciencedirect.com/science/article/pii/S0377027315002735>
- 1322 Pola, A., Crosta, G. B., Fusi, N., and Castellanza, R. (2014). General characterization of the mechanical  
 1323 behaviour of different volcanic rocks with respect to alteration. *Engineering Geology*, 169, 1-13.  
 1324 <http://www.sciencedirect.com/science/article/pii/S0013795213003293>
- 1325 Price, R. C., Gamble, J. A., Smith, I. E. M., Maas, R., Waight, T., Stewart, R. B., and Woodhead, J. (2012).  
 1326 The Anatomy of an Andesite Volcano: a Time–Stratigraphic Study of Andesite Petrogenesis and  
 1327 Crustal Evolution at Ruapehu Volcano, New Zealand. *Journal of Petrology*, 53(10), 2139-2189.  
 1328 <https://doi.org/10.1093/petrology/egs050>
- 1329 Procter, J. N., Cronin, S. J., Zernack, A. V., Lube, G., Stewart, R. B., Nemeth, K., and Keys, H. (2014). Debris  
 1330 flow evolution and the activation of an explosive hydrothermal system; Te Maari, Tongariro,  
 1331 New Zealand. *Journal of Volcanology and Geothermal Research*, 286, 303-316.  
 1332 <http://www.sciencedirect.com/science/article/pii/S0377027314002170>
- 1333 Pu, H.-C., Lin, C.-H., Hsu, Y.-J., Lai, Y.-C., Shih, M.-H., Murase, M., and Chang, L.-C. (2020). Volcano-  
 1334 hydrothermal inflation revealed through spatial variation in stress field in Tatun Volcano Group,  
 1335 Northern Taiwan. *Journal of Volcanology and Geothermal Research*, 390, 106712.  
 1336 <http://www.sciencedirect.com/science/article/pii/S0377027319304093>
- 1337 Pullanagari, R. R., Kereszturi, G., and Yule, I. J. (2016). Mapping of macro and micro nutrients of mixed  
 1338 pastures using airborne AisaFENIX hyperspectral imagery. *ISPRS Journal of Photogrammetry and*  
 1339 *Remote Sensing*, 117, 1-10.  
 1340 <http://www.sciencedirect.com/science/article/pii/S0924271616000782>
- 1341 Reid, M. E. (2004). Massive collapse of volcano edifices triggered by hydrothermal pressurization.  
 1342 *Geology*, 32(5), 373-376. <http://pubs.er.usgs.gov/publication/70027272>
- 1343 Richter, R., and Schläpfer, D. (2002). Geo-atmospheric processing of airborne imaging spectrometry  
 1344 data. Part 2: Atmospheric/topographic correction. *International Journal of Remote Sensing*,  
 1345 23(13), 2631-2649. <http://dx.doi.org/10.1080/01431160110115834>

- 1346 Roberts, D. A., Gardner, M., Church, R., Ustin, S., Scheer, G., and Green, R. O. (1998). Mapping Chaparral  
 1347 in the Santa Monica Mountains Using Multiple Endmember Spectral Mixture Models. *Remote*  
 1348 *Sensing of Environment*, 65(3), 267-279.  
 1349 <http://www.sciencedirect.com/science/article/pii/S0034425798000376>
- 1350 Rogge, D., Rivard, B., Segl, K., Grant, B., and Feng, J. (2014). Mapping of NiCu–PGE ore hosting ultramafic  
 1351 rocks using airborne and simulated EnMAP hyperspectral imagery, Nunavik, Canada. *Remote*  
 1352 *Sensing of Environment*, 152(0), 302-317.  
 1353 <http://www.sciencedirect.com/science/article/pii/S0034425714002442>
- 1354 Rosas-Carbajal, M., Komorowski, J.-C., Nicollin, F., and Gibert, D. (2016). Volcano electrical tomography  
 1355 unveils edifice collapse hazard linked to hydrothermal system structure and dynamics. *Scientific*  
 1356 *Reports*, 6(1), 29899. <https://doi.org/10.1038/srep29899>
- 1357 Rowan, L. C., and Mars, J. C. (2003). Lithologic mapping in the Mountain Pass, California area using  
 1358 Advanced Spaceborne Thermal Emission and Reflection Radiometer (ASTER) data. *Remote*  
 1359 *Sensing of Environment*, 84(3), 350-366.
- 1360 Rowe, G. L., and Brantley, S. L. (1993). Estimation of the dissolution rates of andesitic glass, plagioclase  
 1361 and pyroxene in a flank aquifer of Poás Volcano, Costa Rica. *Chemical Geology*, 105(1), 71-87.  
 1362 <http://www.sciencedirect.com/science/article/pii/0009254193901194>
- 1363 Rowlands, D. P., White, R. S., and Haines, A. J. (2005). Seismic tomography of the Tongariro Volcanic  
 1364 Centre, New Zealand. *Geophysical Journal International*, 163(3), 1180-1194.  
 1365 <https://doi.org/10.1111/j.1365-246X.2005.02716.x>
- 1366 Rutledge, A. M., Horgan, B. H. N., Havig, J. R., Rampe, E. B., Scudder, N. A., and Hamilton, T. L. (2018).  
 1367 Silica Dissolution and Precipitation in Glaciated Volcanic Environments and Implications for  
 1368 Mars. *Geophysical Research Letters*, 45(15), 7371-7381.  
 1369 <https://agupubs.onlinelibrary.wiley.com/doi/abs/10.1029/2018GL078105>
- 1370 Rye, R. O. (2005). A review of the stable-isotope geochemistry of sulfate minerals in selected igneous  
 1371 environments and related hydrothermal systems. *Chemical Geology*, 215(1), 5-36.  
 1372 <http://www.sciencedirect.com/science/article/pii/S0009254104003869>
- 1373 Rye, R. O., Bethke, P. M., and Wasserman, M. D. (1992). The stable isotope geochemistry of acid sulfate  
 1374 alteration. *Economic Geology*, 87(2), 225-262. <https://doi.org/10.2113/gsecongeo.87.2.225>
- 1375 Schaefer, L. N., Kendrick, J. E., Oommen, T., Lavallée, Y., and Chigna, G. (2015). Geomechanical rock  
 1376 properties of a basaltic volcano. *Frontiers in Earth Science*, 3(29). Original Research.  
 1377 <http://journal.frontiersin.org/article/10.3389/feart.2015.00029>
- 1378 Schaefer, L. N., Kennedy, B. M., Villeneuve, M. C., Cook, S. C. W., Jolly, A. D., Keys, H. J. R., and Leonard,  
 1379 G. S. (2018). Stability assessment of the Crater Lake/Te Wai-ā-moe overflow channel at Mt.  
 1380 Ruapehu (New Zealand), and implications for volcanic lake break-out triggers. *Journal of*  
 1381 *Volcanology and Geothermal Research*, 358, 31-44.  
 1382 <http://www.sciencedirect.com/science/article/pii/S0377027318301008>
- 1383 Schläpfer, D., and Richter, R. (2002). Geo-atmospheric processing of airborne imaging spectrometry  
 1384 data. Part 1: Parametric orthorectification. *International Journal of Remote Sensing*, 23(13),  
 1385 2609-2630. <http://dx.doi.org/10.1080/01431160110115825>
- 1386 Schwertmann, U., and Murad, E. (1983). Effect of pH on the Formation of Goethite and Hematite from  
 1387 Ferrihydrite. *Clays and Clay Minerals*, 31(4), 277-284. journal article.  
 1388 <https://doi.org/10.1346/CCMN.1983.0310405>
- 1389 Scott, K. M. (1990). Origin of alunite- and jarosite-group minerals in the Mt. Leyshon epithermal gold  
 1390 deposit, Northeast Queensland, Australia. *American Mineralogist*, 75(9-10), 1176-1181.
- 1391 Sillitoe, R. H., and Hedenquist, J. W. (2003). Linkages between volcanotectonic settings, ore-fluid  
 1392 compositions, and epithermal precious metal deposits. *Special Publication-Society of Economic*  
 1393 *Geologists*, 10, 315-343.

- 1394 Simmons, S. F., White, N. C., John, D. A., Hedenquist, J. W., Thompson, J. F. H., Goldfarb, R. J., and  
 1395 Richards, J. P. (2005). Geological Characteristics of Epithermal Precious and Base Metal Deposits.  
 1396 In *One Hundredth Anniversary Volume* (pp. 0): Society of Economic Geologists.
- 1397 Siratovich, P. A., Heap, M. J., Villeneuve, M. C., Cole, J. W., Kennedy, B. M., Davidson, J., and Reuschlé, T.  
 1398 (2016). Mechanical behaviour of the Rotokawa Andesites (New Zealand): Insight into  
 1399 permeability evolution and stress-induced behaviour in an actively utilised geothermal reservoir.  
 1400 *Geothermics*, 64, 163-179.  
 1401 <http://www.sciencedirect.com/science/article/pii/S0375650516300451>
- 1402 Smith, D. J., Naden, J., Jenkin, G. R. T., and Keith, M. (2017). Hydrothermal alteration and fluid pH in  
 1403 alkaline-hosted epithermal systems. *Ore Geology Reviews*, 89, 772-779.  
 1404 <http://www.sciencedirect.com/science/article/pii/S0169136817302913>
- 1405 Stern, T. A., Stratford, W. R., and Salmon, M. L. (2006). Subduction evolution and mantle dynamics at a  
 1406 continental margin: Central North Island, New Zealand. *Reviews of Geophysics*, 44(4).  
 1407 <https://agupubs.onlinelibrary.wiley.com/doi/abs/10.1029/2005RG000171>
- 1408 Stoffregen, R. E., and Alpers, C. N. (1987). Woodhouseite and svanbergite in hydrothermal ore deposits;  
 1409 products of apatite destruction during advanced argillic alteration. *The Canadian Mineralogist*,  
 1410 25(2), 201-211.
- 1411 Streck, M. J., and Dilles, J. H. (1998). Sulfur evolution of oxidized arc magmas as recorded in apatite from  
 1412 a porphyry copper batholith. *Geology*, 26(6), 523-526. [https://doi.org/10.1130/0091-](https://doi.org/10.1130/0091-7613(1998)026<0523:SEOOAM>2.3.CO;2)  
 1413 [7613\(1998\)026<0523:SEOOAM>2.3.CO;2](https://doi.org/10.1130/0091-7613(1998)026<0523:SEOOAM>2.3.CO;2)
- 1414 Swayze, G. A., Clark, R. N., Goetz, A. F. H., Livo, K. E., Breit, G. N., Kruse, F. A., et al. (2014). Mapping  
 1415 Advanced Argillic Alteration at Cuprite, Nevada, Using Imaging Spectroscopy. *Economic Geology*,  
 1416 109(5), 1179-1221. <http://economicgeology.org/content/109/5/1179.abstract>
- 1417 Ta, K., Peng, X., Chen, S., Xu, H., Li, J., Du, M., et al. (2017). Hydrothermal nontronite formation  
 1418 associated with microbes from low-temperature diffuse hydrothermal vents at the South Mid-  
 1419 Atlantic Ridge. *Journal of Geophysical Research: Biogeosciences*, 122(9), 2375-2392.
- 1420 Tan, W., Liu, P., He, H., Wang, C. Y., and Liang, X. (2016). Mineralogy and Origin of Exsolution in Ti-rich  
 1421 Magnetite from Different Magmatic Fe-ti Oxide-bearing Intrusions. *The Canadian Mineralogist*,  
 1422 54(3), 539-553. <https://doi.org/10.3749/canmin.1400069>
- 1423 Tost, M., Cronin, S. J., Procter, J. N., Smith, I. E. M., Neall, V. E., and Price, R. C. (2015). Impacts of  
 1424 catastrophic volcanic collapse on the erosion and morphology of a distal fluvial landscape:  
 1425 Hautapu River, Mount Ruapehu, New Zealand. *Geological Society of America Bulletin*, 127(1-2),  
 1426 266-280. <http://gsabulletin.gsapubs.org/content/127/1-2/266.abstract>
- 1427 Townsend, D. B., Leonard, G. S., Conway, C. E., Eaves, S. R., Wilson, C. J. N., and compilers. (2017).  
 1428 Geology of the Tongariro National Park area [scale 1:60 000 map]. In *GNS Science geological*  
 1429 *map*; 4 (pp. 1 sheet + 109 p., ). Lower Hutt, New Zealand: GNS Science.
- 1430 van der Meer, F. (2004). Analysis of spectral absorption features in hyperspectral imagery. *International*  
 1431 *Journal of Applied Earth Observation and Geoinformation*, 5(1), 55-68.  
 1432 <http://www.sciencedirect.com/science/article/pii/S0303243403000382>
- 1433 van der Meer, F., Kopačková, V., Koucká, L., van der Werff, H. M. A., van Ruitenbeek, F. J. A., and Bakker,  
 1434 W. H. (2018). Wavelength feature mapping as a proxy to mineral chemistry for investigating  
 1435 geologic systems: An example from the Rodalquilar epithermal system. *International Journal of*  
 1436 *Applied Earth Observation and Geoinformation*, 64, 237-248.  
 1437 <http://www.sciencedirect.com/science/article/pii/S0303243417301976>
- 1438 van Hinsberg, V., Berlo, K., van Bergen, M., and Williams-Jones, A. (2010). Extreme alteration by  
 1439 hyperacidic brines at Kawah Ijen volcano, East Java, Indonesia: I. Textural and mineralogical  
 1440 imprint. *Journal of Volcanology and Geothermal Research*, 198(1), 253-263.  
 1441 <http://www.sciencedirect.com/science/article/pii/S037702731000288X>

- 1442 Vasconcelos, P. M., and Conroy, M. (2003). Geochronology of weathering and landscape evolution,  
1443 Dugald River valley, NW Queensland, Australia. *Geochimica et Cosmochimica Acta*, 67(16), 2913-  
1444 2930. <http://www.sciencedirect.com/science/article/pii/S0016703702013728>
- 1445 Wallace, L. M., Beavan, J., McCaffrey, R., and Darby, D. (2004). Subduction zone coupling and tectonic  
1446 block rotations in the North Island, New Zealand. *Journal of Geophysical Research: Solid Earth*,  
1447 109(B12). <https://agupubs.onlinelibrary.wiley.com/doi/abs/10.1029/2004JB003241>
- 1448 Watters, R. J., Delahaut, W. D., Haneberg, W. C., and Anderson, S. A. (1995). Effect of argillic alteration  
1449 on rock mass stability. In *Clay and Shale Slope Instability* (Vol. 10, pp. 0): Geological Society of  
1450 America.
- 1451 Westoby, M. J., Brasington, J., Glasser, N. F., Hambrey, M. J., and Reynolds, J. M. (2012). 'Structure-from-  
1452 Motion' photogrammetry: A low-cost, effective tool for geoscience applications.  
1453 *Geomorphology*, 179, 300-314.  
1454 <http://www.sciencedirect.com/science/article/pii/S0169555X12004217>
- 1455 Wright, R., Flynn, L. P., and Harris, A. J. L. (2001). Evolution of lava flow-fields at Mount Etna, 27-28  
1456 October 1999, observed by Landsat 7 ETM+. *Bulletin of Volcanology*, 63(1), 1-7.  
1457 [http://www.scopus.com/inward/record.url?eid=2-s2.0-  
1458 0034925245&partnerID=40&md5=a47b808c2afe4cd05f7e7792e9a9d6af](http://www.scopus.com/inward/record.url?eid=2-s2.0-0034925245&partnerID=40&md5=a47b808c2afe4cd05f7e7792e9a9d6af)
- 1459 Wyering, L. D., Villeneuve, M. C., Wallis, I. C., Siratovich, P. A., Kennedy, B. M., Gravley, D. M., and Cant,  
1460 J. L. (2014). Mechanical and physical properties of hydrothermally altered rocks, Taupo Volcanic  
1461 Zone, New Zealand. *Journal of Volcanology and Geothermal Research*, 288, 76-93.  
1462 <http://www.sciencedirect.com/science/article/pii/S0377027314003060>
- 1463 Zabcic, N., Rivard, B., Ong, C., and Mueller, A. (2014). Using airborne hyperspectral data to characterize  
1464 the surface pH and mineralogy of pyrite mine tailings. *International Journal of Applied Earth  
1465 Observation and Geoinformation*, 32(0), 152-162.  
1466 <http://www.sciencedirect.com/science/article/pii/S0303243414000920>
- 1467 Zimbelman, D. R., Rye, R. O., and Breit, G. N. (2005). Origin of secondary sulfate minerals on active  
1468 andesitic stratovolcanoes. *Chemical Geology*, 215(1), 37-60.  
1469 <http://www.sciencedirect.com/science/article/pii/S0009254104003870>
- 1470 Zolotov, M. Y., and Shock, E. L. (2005). Formation of jarosite-bearing deposits through aqueous oxidation  
1471 of pyrite at Meridiani Planum, Mars. *Geophysical Research Letters*, 32(21).  
1472 <https://agupubs.onlinelibrary.wiley.com/doi/abs/10.1029/2005GL024253>
- 1473